LAWRENCE
LIVERMORE
NATIONAL
LABORATORY

LLNL-JRNL-406569

Shocked Materials at the Intersection of Experiment and Simulation

H. Lorenzana, J. F. Belak, K. S. Bradley, E. M. Bringa, K. S. Budil, J. U. Cazamias, B. El-Dasher, K. Kadau, D. H. Kalantar, J. A. Hawreliak, J. Hessler, J. M. McNaney, D. Milathianaki, K. Rosolankova, D. C. Swift, M. Taravillo, T. W. Van Buuren, J. S. Wark, T. Diaz De La Rubia

August 26, 2008

Scientific Modeling and Simulation

Disclaimer

This document was prepared as an account of work sponsored by an agency of the United States government. Neither the United States government nor Lawrence Livermore National Security, LLC, nor any of their employees makes any warranty, expressed or implied, or assumes any legal liability or responsibility for the accuracy, completeness, or usefulness of any information, apparatus, product, or process disclosed, or represents that its use would not infringe privately owned rights. Reference herein to any specific commercial product, process, or service by trade name, trademark, manufacturer, or otherwise does not necessarily constitute or imply its endorsement, recommendation, or favoring by the United States government or Lawrence Livermore National Security, LLC. The views and opinions of authors expressed herein do not necessarily state or reflect those of the United States government or Lawrence Livermore National Security, LLC, and shall not be used for advertising or product endorsement purposes.

Shocked Materials at the Intersection of Experiment and Simulation

H. E. Lorenzana[*], J. F. Belak[*], K. S. Bradley[*], E. M. Bringa[*], K. S. Budil[*], J. U. Cazamias[†], B. El-Dasher[*], K. Kadau[**], D. H. Kalantar[*], J. A. Hawreliak[*], J. Hessler[††], J. M. McNaney[*], D. Milathianaki[*], K. Rosolankova[‡], D. C. Swift[*], M. Taravillo[§], T. W. Van Buuren[*], J. S. Wark[‡], and T. Diaz De La Rubia[*]

[*]*Lawrence Livermore National Laboratory, 7000 East Avenue, Livermore, CA, USA*
[**]*Los Alamos National Laboratory, Los Alamos, NM USA*
[†]*Army Research Laboratory, Aberdeen, MD, USA*
[††]*Argonne National Laboratory, Argonne, IL USA*
[‡]*University of Oxford, Oxford, United Kingdom*
[§]*Universidad Complutense de Madrid, Madrid, Spain*

Abstract Understanding the dynamic lattice response of solids under the extreme conditions of pressure, temperature and strain rate is a scientific quest that spans nearly a century. Critical to developing this understanding is the ability to probe and model the spatial and temporal evolution of the material microstructure and properties at the scale of the relevant physical phenomena—nanometers to micrometers and picoseconds to nanoseconds. While experimental investigations over this range of spatial and temporal scales were unimaginable just a decade ago, new technologies and facilities currently under development and on the horizon have brought these goals within reach for the first time. The equivalent advancements in simulation capabilities now mean that we can conduct simulations and experiments at overlapping temporal and spatial scales. In this article, we describe some of our studies which exploit existing and new generation ultrabright, ultrafast x-ray sources and large scale molecular dynamics simulations to investigate the real-time physical phenomena that control the dynamic response of shocked materials.

Shock • Phase Transformations • Damage • Shock Diagnostic Tools • Molecular Dynamics Materials Simulation • Ultrafast phenomena

1 Introduction

Materials dynamics, particularly the behavior of solids under extreme dynamic compression, is a topic of broad scientific and technological interest [Meyers 1994; Davidson 2002]. It is well-established that the bulk material response is strongly dependent on the processing history and is affected by physical processes that encompass a wide range of temporal and spatial scales [Asay 1997]. In this work, we consider the lattice-level response of a solid to shock compression. It is widely accepted that the material morphology and timescales of atomistic phenomena have a profound impact on bulk properties, such as plasticity, phase transformations, and damage [Preston 2002]. Yet, despite the acknowledged importance of these ultrafast microscopic processes, few studies have cast light on their nature or provided details of how they govern material response during the passage of the shock.

Consider a notional crystalline solid, as illustrated in Fig. 1.1. In the case of a planar shock denoted here, the initial response is a compression of the crystal along lattice planes whose unit normals are partially aligned with the direction of shock propagation. This uniaxial response can remain elastic; that is, once the disturbance is removed, the lattice will relax back to its original configuration. However, under high-stress conditions and given sufficient time, the lattice will undergo an irreversible response. The local nucleation and kinetics of defects and phases leads to plasticity, melting, resolidification, or solid-solid structural transformations. These atomistic changes can have dramatic and important consequences to most macroscopically observable behavior such as the material's thermodynamic state (pressure, temperature, density), strength, and failure. Little or no data exists concerning the nature of defect generation and mobility, phase nucleation and growth, and void formation under these highly dynamic stress conditions.

Historically, two approaches have been employed to address this lack of data: sample recovery [Smith 1958] and in situ bulk property measurements. The first approach emphasizes microstructural analysis but does not allow direct probing of the samples under dynamic loading. The examination of shock recovered specimens provides end-state information that can be useful in *inferring* dynamic behavior [Meyers 2003, Schneider 2004]. In the second approach, real-time measurements of the bulk response are recorded with fast diagnostics such as surface velocimetry (VISAR) and internal stress gauges [Duff 1957]. While such approaches have proven themselves to be valuable and are largely responsible for our current understanding, these continuum level methodologies are limited in the insight that they can provide about lattice level processes under dynamic conditions. As an illustration of this point, a phase transformation event and its kinetics are inferred from the change in slope of the VISAR wave profile in Fig. 1.1, effectively measuring a change in the compressibility of the material but providing no insight as to the atomic level details.

It is clear that a fundamental understanding requires the direct probing and study of relevant, transient physical processes at their characteristic lattice length scales. We are at a unique crossroad in materials science where theory, experiments, and simulations have progressed to the point that such investigations at overlapping temporal and spatial scales are now possible. This manuscript describes some of our efforts enabled by new advances in the technology of ultrabright, pulsed x-ray sources and massively parallel computation. We describe two classes of experimental approaches: laser-based, which offer seamless timing precision and proven shock loading capabilities, and accelerator-based, which possess unparalleled x-ray beam quality and brightness for diagnostics. These approaches are complementary in their capacity to probe from the nano-to-macroscale in the spatial and picosecond-to-nanosecond in the temporal regimes. We discuss our recent experiments and simulations, casting light on elastic-to-plastic relaxation and solid-solid phase transformations during the shock. We also introduce future areas of investigation of melt and damage phenomena under dynamic compression conditions.

2 Approaches to In Situ Studies of Atomic Processes Under Dynamic Compression

It is now routine to subject macroscopic samples (~ 0.1 mm to 1 cm) to energy densities exceeding 10^{12} ergs/cm^3 (~100 GPa pressures) using high-energy laser and multiple-stage gas guns. Experiments are currently being designed to investigate solids at pressures significantly exceeding 100 GPa at ultrafast timescales using next generation high energy density (HED) facilities, such as the National Ignition Facility (NIF at Lawrence Livermore National Laboratory) and the Linac Coherent Light Source (LCLS at Stanford University) [Cornacchia 2004, Remington 2005]. In parallel, computational MD methodologies have now progressed to the point where the simulation of ~μm size samples out to ~100 ps is now possible using state-of-the-art computers [Bringa 2005]. Because of the extreme challenges in conducting experiments under HED conditions, insight into the atomistic response of the solid under shock conditions has been limited. We now briefly outline both the experimental and computational approaches used in this work to perform the real-time and in situ investigations of the dynamic material processes.

2.1 X-ray techniques—Diffraction and Scattering

X-ray diffraction and scattering provide a non-perturbative probe into the lattice level response of the shocked solid [d'Almeida 2000, Kalantar 1999]. Diffraction in solids relies on the coherent scattering of x-rays from a periodic array of atoms to produce spectra that can be correlated with the atomic structure and described by Bragg's law. X-ray scattering, on the other hand, is sensitive to the larger-scale density variations associated with void nucleation and growth. In principle, temporal resolution of shock loading can be obtained through two basic approaches: (a) gating or streaking the detector and/or (b) pulsing the x-ray probe. The first approach in principle could be implemented to as fast as 50 ps with a narrow field of view but has been demonstrated to ~50 ns resolutions in gas gun experiments [Johnson 1972, Rigg 1998] with 2 to 4 ns resolution when streaked [Rigg 2003]. In contrast, current state-of-the-art, pulsed x-ray studies are sub-nanosecond with the ability to use wide-angle detectors [Kalantar 2000, Wark 1989]. Femtosecond resolution is on the horizon with the development of new accelerator-based sources.

Laser-Based Systems For X-ray Diffraction: Current high-energy laser facilities have been shown to be excellent venues to generate both high pressure loading [Boustie 1996, Romain 1986, Colvin 2003] and implement x-ray-based diagnostics [Ochi 2003]. Shock pressures between 10 and 1000 GPa are easily accessible through direct ablative drive. Temporal variation of the drive can be tailored by either laser pulse shaping or target design, while spatial uniformity of the drive is ensured through the use of phase plates. Recently, quasi-isentropic drives capable of producing shockless loading have been demonstrated at pressures between 10 and 200 GPa [Edwards 2004, Lorenz 2005]. This shockless loading is expected to allow access to strain rates from as low as 10^6 sec^{-1} up to the shock regime > 10^{10} sec^{-1}. Laser sources can also thermally excite a wide range of x-ray source characteristics from inner core atomic transitions [Phillion 1986]. Source fluence can exceed 10^{15} photons/pulse of isotropically illuminating x-rays, orders of magnitude larger than the $\sim 10^9$ photons required for single-pulse x-ray diffraction, with energies in the range of 500 eV to 22 keV [Park 2008].

Multi-beam laser facilities provide exquisite control over timing between drive and diagnostic functions. A typical experimental geometry, as illustrated in Fig. 2.1, offers a largely unobstructed experimental view for large-area x-ray detectors [Kalantar 2003, Swift 2001, Wark 1989]. The sample is driven by a set of coordinated laser pulses that launch a shock into the sample at pressure $P \sim I_L^{2/3}$, where I_L is the laser intensity [Lindl 1995]. A separate set of beams are used to generate a thermal plasma via laser heating that serves as a point source of diagnostic x-rays, termed a backlighter. To provide the time evolution measurements, these x-rays are delayed relative to the beams that drive the shock. The backlighting beams are of ~1 ns duration and are short enough to effectively freeze some of the lattice dynamics of interest in each image. The lattice compression shifts the angle at which the diffracted signal is observed, as shown in Fig. 2.1. This separation of signal in angle and space makes it possible to perform a measurement in which both the shocked and unshocked states of the crystal can be diagnosed simultaneously. The detector for these measurements covers a large field of view, allowing for the collection of diffraction from multiple lattice planes.

Accelerator-Based Light Source For X-ray Scattering: Synchrotrons have traditionally offered significant advantages for x-ray experiments including brightness, monochromaticity, coherence, collimation, and stability. Synchrotron radiation is pulsed, since the electrons in the storage ring are bunched, and thus can be used to generate ultrashort, ultrabright pulses of x-rays for time-resolved measurements. To optimize the timing and brightness for pump-probe experiments, the storage ring fill pattern can be adjusted to run in a hybrid mode which consists of a single isolated electron bunch separated in time from a train of bunches. Such fill patterns can change the timing between electron bunches to the order of microseconds and allow the use of gated cameras to time-resolve signals. We note that the time resolution is currently ~ 100 picosecond (sub-nanosecond) but soon, with the development of fourth generation synchrotrons, is expected to be ~100 femtoseconds [Kim 2005].

Computation-Simulation: Molecular dynamics (MD) simulations solve the equations of motion for a set of atoms mediated by interatomic potentials [Holian 1998]. Such interatomic potentials are generated by fitting to a data bank of electronic structure calculations for the energies and atomic forces of relevant crystal structures. For our purposes, samples are prismatic with free surfaces parallel and periodic boundary conditions perpendicular to the shock direction. The first few surface layers on one of the free surfaces are taken to act as a piston and constrained to move at a constant or ramped velocity. At each time step, the stress and strain state, local phase and dislocation densities can be extracted.

Post-processing these simulations allows the calculation of the expected x-ray diffraction and scattering signals [Rosolankova 2005, Rosolankova 2006]. To simulate these observables, we perform a Fourier transform on the calculated atomic positions. Since the positions of the atoms are given by arbitrary and not discretized x, y, and z coordinates, special techniques are required to take advantage of fast Fourier transform methods, which are not discussed here. We calculate the Fourier transform using

$$I(\vec{k}) = \left| \sum_{n=0}^{N-1} e^{-i(\vec{k}\cdot\vec{r}_n)} \right|^2$$

where r_n is the position of the nth atom and N is the total number of atoms in a given test volume or crystal. The solution to this equation for a lattice of atoms is a periodic distribution of intense scattering peaks in k-space. The location of these resonances is given by $\vec{k} = h\vec{b}_1 + k\vec{b}_2 + l\vec{b}_3$ where $\vec{b}_n$ (n=1,2,3) are the reciprocal lattice vectors that define the crystallography and *(h,k,l)* are the standard Miller indices that describe the diffraction plane.

Modeling simulated x-ray scattering in this fashion has three distinct and important advantages. First, it provides a method for analyzing the vast amounts of output from an MD simulation. The location and intensity of the spots can be used to determine atomic structure, and more subtle features, like broadening and shifts, can give information about dislocation density through techniques applied to standard high resolution x-ray diffraction experiments. Second, it allows for the optimization of future experiments by identifying specific physical phenomena and relevant experimental conditions to target for investigation. Last, but potentially most important, it allows a direct comparison between experiment and simulation. Good agreement provides higher confidence in the simulations yielding enhanced understanding of the measured lattice kinetics and generating improved potentials.

3 Materials Response to Shock Loading

3.1 Inelastic Response to Shock Loading (1D to 3D Transition)

The initial response of a crystalline material to shock loading is uniaxial, elastic compression (1D), leading to a strong shear stress on the lattice. If the shock wave propagating through the lattice exceeds the Hugoniot elastic limit (HEL), this shear stress leads to nucleation of dislocations, allowing the lattice to plastically relax to a more quasi-hydrostatic compression (3D) on some characteristic timescale. The rate of relaxation to hydrostatic conditions is controlled by the nucleation rates and mobility of dislocations, which in turn depend upon microstructural parameters such as grain boundaries, barriers, etc.

Experimentally, this relaxation of the lattice behind a shock has been studied with time-resolved diffraction for FCC metals. As an example, such kinetics have been studied in single crystal copper shocked to 18 GPa. [Loveridge-Smith 2001]. The degree of lattice relaxation was determined through diffraction recorded from (200) planes both parallel and perpendicular to the shock loading direction. These samples were found to have approached a 3D state in less than 400 ps after the passage of the shock front. These observations in copper are broadly supported by results from our MD simulations [Bringa 2006], which are discussed next and show relaxation occurring over a period of less than 100 ps

With the advent of large-scale MD simulations, we can now directly compare results from simulations to time-resolved in-situ x-ray diffraction experiments. The simulations used a ~1 μm long single crystal copper comprised of up to 352 million atoms as the starting material with pre-existing dislocation sources in the form of prismatic dislocation loops. Two large scale MD simulations were conducted, both with a peak piston velocity of U_p=0.75 km s^{-1} (peak pressures of approximately 35 GPa) but with different loading profiles. One simulation ramped the piston to the peak velocity over 50 ps while the other used an instantaneous "shock" loading. The ramped velocity was aimed at forming a link to experiments, which have shown rise times ranging from several picoseconds to several nanoseconds. A snapshot of both simulations at 100 ps shows a large dislocation network in Fig. 3.1.1. The 0 ps rise time shows only homogeneous nucleation (Fig. 3.1.1a), while the 50ps rise time exhibits three regions of dislocation activity (Fig. 3.1.1b).

The total dislocation density (ρ_d) versus depth is plotted for 100 ps in Fig. 3.1.1c. The zero rise-time case saturates at a steady-state value of $3x10^{13}$ cm^{-2}. This value is very large compared with the density of pre-existing sources or the dislocation density typically found in shock recovered samples [Meyers 2003]. Interestingly, we observe that the final state and microstructure in the 0 ps rise time simulations appeared not to be affected by the initial defect concentration. In contrast, for the ramped case, the pre-existing defects led to significant dislocation multiplication and partial stress relaxation throughout the simulated sample.

A fully 3D relaxed state is ideally defined as having zero shear stress and hydrostatic compression. Fig. 3.1.2 shows that the shear stress behind the shock front markedly decreases over approximately 60 ps for both types of loadings with more than half of shear stress relieved within ~10 ps after the shock passage. The shear stress evolves to an asymptotic value of 0.43 GPa for the zero rise-time simulation and 0.34 GPa for the ramped loading simulation and is comparable to that inferred from the in situ diffraction experiments on copper [Meyers 2003]. Using the MD simulation, we calculated the expected x-ray diffraction pattern. We analyzed such patterns with tools used to quantify lattice changes in experimental data. These results are summarized in Fig. 3.1.3, which indicate significant lateral relaxation only at times much greater than 10 ps. Due to the significant stress relaxation that has occurred, the simulated X-ray diffraction shows nearly uniform 3D compression, i.e. 5% in each direction. These large scale simulations are the first to capture the scope of this lattice relaxation, as previous work was limited to timescales of ~10 ps, too short to follow fully the evolution.

On the basis of our simulations, we can anticipate two interesting implications for future experiments. The first is that relaxation phenomena in copper can be observed only at the picosecond timescale, with little or no relaxation expected until after ~10 ps after shock passage. This suggests that we would need to experimentally probe with picosecond resolution, currently an experimental challenge. The second is that the influence of pre-existing defects on the final microstructure should be negligible for strong shocks above the limit for homogeneous nucleation of dislocations. This latter observation poses a testable prediction that can be addressed by appropriate selection of drive conditions and engineering of the initial microstructure of samples.

While copper is an example of an FCC material that shows ultrafast plastic relaxation, iron is a BCC material that exhibits notably longer timescale kinetics for plasticity and appears to be sensitive to the starting microstructure. Iron MD simulations performed by Kadau et al. [Kadau 2002] generated a shock by using the momentum mirror method [Holian 1998] and relied on periodic boundary conditions in the lateral directions (x and y). The duration of each simulation was 10 ps, the time taken for the shock to transit the 80 nm simulated single crystal. This work predicted the $\alpha-\varepsilon$ transition under shock compression at a pressure of just over 15 GPa, reasonably consistent with gas gun experiments [Boettger 1997].

Using these MD simulations, we calculated the expected x-ray diffraction pattern for single crystal iron. As evident from Fig. 3.1.4, there was no lattice relaxation observed below the transition on the timescale of the simulations. The generation and motion of dislocations associated with plastic flow would have resulted in both a reduction in the mean lattice parameter perpendicular to the shock propagation direction and an expansion of the reciprocal lattice, which were not observed.

For highly pure, melt-grown single crystals, the experimental results are consistent with the simulation, namely that no lattice relaxation is observed before the onset of the phase transition (data shown later in Fig. 3.2.5). For data at 12 GPa just below the transition, the diffraction lines associated with the (002), (112), and $(1\bar{1}2)$ indicate a compression along the shock direction of 5.2% based on the change in diffraction of the (002) plane. The lateral deformation, in contrast, can be estimated at 0.0%+/- 0.6% based on the (112) and $(1\bar{1}2)$ planes. A similar analysis of data recorded at 13 GPa shows compression in the shock direction of 5.8% +/- 0.3% with the lateral compression estimated to be 0.0% +/- 0.6% based on the same diffraction planes [Hawreliak 2006]. Within the uncertainty of the measurement, the experiments demonstrate only uniaxial, elastic compression before the phase transition, which agrees well with the MD simulations. We note two key points and differences: first that the experimental observations are made on a timescale that are approximately a nanosecond or two orders of magnitude longer than that of the simulation, and second, that the measured pressure far exceeds the accepted HEL.

This nanosecond elastic response of iron all the way up to the transition pressure of 12 GPa contrasts with the plastic behavior inferred from continuum wave profiles of shocked iron at the microsecond timescales [Bancroft 1956, Kozlov 2005]. In continuum experiments, a three-wave structure is often observed—the first being associated with the HEL, the second with an elastic-plastic transition, and the final with the phase transition itself. While further work is needed to understand the elastic behavior in iron vis-à-vis the plastic response at different timescales, we can outline two important conclusions from the existing work that begin to address this complicated scientific area.

First, we note that the laser experiments are at a time scale intermediate between the picosecond MD simulations and microsecond shock-wave experiments. Because we see no plastic response in high-quality single crystals, it is evident that our laser-based results are serving as an valuable window into the nucleation and mobility of defects under shock, as both these processes play key roles in sample relaxation. We conclude that the combined kinetics of these phenomena appear to be longer than ~1 ns.

Second, our results also indicate that the elastic/plastic response in iron appears to be significantly affected by the initial microstructure of the sample itself. Most previous work on iron has focused on polycrystalline samples, while the diffraction experiments described here utilized single crystals. En route to systematically identifying the effect of microstructure, we have studied two kinds of single-crystal iron samples in this work, thick samples (~400 of μm) grown from a melt process and thin samples (~10 μm) vapor deposited onto a single crystal substrate. Perhaps surprisingly, the diffraction patterns from the vapor deposited samples exhibited lattice relaxation at a timescale faster than the ~1 ns probe. At 11 GPa, the vapor deposited samples show a compression of 3.8% +/- 0.2% of the (002) plane along the shock direction a 2.8% +/- 0.6% compression of (112), $(\bar{1}\bar{1}2)$, (110) and (020) planes in the lateral direction, exhibiting a degree of plastic deformation [Hawreliak 2006]. We speculate that the difference between the elastic response for melt grown and plastic behavior for vapor deposited crystals is due to the lower crystalline quality of the latter samples.

Results such as outlined here are only now beginning to provide some insight into the atomistic processes that control the evolution of the shocked solid. It is clear that substantial work remains in order to understand the complicated and interrelated effects of the initial state of the crystals, the temporal and spatial drive characteristics, strain rate, temperature, sample size, and other parameters on the dynamic plastic response of the shocked solid.

3.2 Phase Transformations

Few properties of the ordered solid are as fundamental and important as its crystallographic structure. The ramifications of the crystal phase are multifold, fundamentally affecting thermodynamic behavior, electronic structure, shock response, strength, and many other properties. Under shock compression, solids generally exhibit a rich gamut of solid-to-solid phase transformations, some of which are metastable and, due to the uniaxial and ultrafast nature of the compression, may differ from those under longer timescale and more hydrostatic conditions. Carbon, for example, demonstrates a wide range of structural states along the Hugoniot, including cubic, hexagonal, nanocrystalline, and amorphous diamond [Bundy 1996, Yamada 2000]. Melting, or solid-to-fluid transformations can also occur under sufficiently strong shocks.

Shock-induced phase transitions represent a fruitful scientific research area where material kinetics can play a key role. One of the most well known and widely studied of these shock-induced transformations is the $\alpha-\varepsilon$ transition in iron, where the BCC α transforms to hexagonal close-packed (HCP) ε structure. This transition was initially discovered in shock compression work done by Bancroft [Bancroft 1956]. These researchers associated the splitting of velocity waves with the elastic-plastic response and the subsequent transformation of iron to a different phase. Analysis of the wave profiles implied that the onset of the phase transition occurred at a pressure of 13 GPa. At that time, the crystallographic structure of this identified phase in iron was unknown. Subsequent static high-pressure x-ray diffraction measurements of iron showed a transformation at about 13 GPa from the BCC to the HCP structure [Mao 1967], which has been assumed to be the same transition as in shock experiments due to the coincidence in pressure. Recently, iron was the first metal studied with dynamic x-ray diffraction techniques to establish the high pressure phase in-situ [Kalantar 2005, Hawreliak 2006]. Some of this work is outlined here.

Phase Transition Pathways: We now discuss two candidate transformation pathways from the high pressure BCC to HCP phase in iron. These phases have certain transformation relations that were first pointed out by Burgers [Burgers 1934]. Specifically, the $(0002)_{HCP}$ basal planes in ε phase HCP structure correspond to what were $(110)_{BCC}$ planes in the low pressure BCC phase. Similarly we find the $[2110]_{HCP}$ axis is aligned with the original $[001]_{BCC}$ axis, $[0002]_{HCP}$ with $[110]_{BCC}$ and $(2110)_{HCP}$ with $(002)_{BCC}$. The exact alignment of these orientations relative to the initial crystal depends on the detailed pathways of the transition. Figures 3.2.1 and 3.2.2 give a description of the two pathway mechanisms being compared in this discussion [Wang 1998]. One mechanism consists of a compression and shuffle that yields alignment between the low pressure BCC and high pressure HCP planes. Described in detail in Fig. 3.2.1, this mechanisms involves a compression along the [001] direction accompanied by an expansion in [110] to generate a hexagon, followed by a shuffle to cause the period doubling for the HCP structure. The other possible mechanism involves a shear and shuffle that introduces a rotation between the corresponding lattice planes, described in Fig. 3.2.2 as a shear and slip mechanism that generates a hexagon with a rotation relative to the corresponding BCC planes.

Phase Transition under Uniaxial Shock Compression Along $[001]_{BCC}$: In the case of uniaxial shock compression along a particular crystallographic direction, the atomic rearrangements required to reach a HCP structure may be influenced by the anisotropies induced by uniaxial compression. In the case of the compressive mechanism illustrated in Fig. 3.2.1, there is no expected change in the transformation pathway as the compression can continue along the uniaxial direction to peak compression without requiring any change in the lateral direction. In contrast, there is marked change to the slip/shear mechanism in Fig. 3.2.2, as the initial uniaxial compression will change the needed rotation to get from the BCC to HCP state during the initial shear. The amount of rotation is shown in Figure 3.2.2b. Static diamond anvil cell experiments using extended x-ray absorption fine structure measurements have indicated a 5° rotation is needed [Wang 1998]. Due to the cubic symmetry of the BCC lattice and the cylindrical symmetry imposed by the uniaxial compression of the shock, both transition mechanisms have degenerate crystallographic directions for the end state. There are four degenerate pathways leading to two distinguishable states for the compressive mechanism, whereas the slip shear mechanism has 4 degenerate states that are all distinguishable.

Calculated Observables for the $\alpha-\varepsilon$ Phase Transition: We now discuss predictions from the simulations that can be directly compared to experimental observations, specifically crystal rotations and volume changes.

Postprocessing of iron MD simulations performed by Kadau et al. [Kadau 2002], as shown in Figs. 3.1.4 and 3.2.3, yields calculated reciprocal lattice space corresponding to the uniaxially compressed BCC lattice. We observe that the BCC lattice reaches a maximum uniaxial compression of 7.0 ± 0.5% for all of the simulations. In contrast, the $(002)_{BCC}$ HCP peak varies in our simulations from 11.5 to 17.4±0.5% compression upon transition to the HCP phase. These compressions, deduced from the shift of the spots in reciprocal space, agree with the direct density measurements from the simulations obtained trivially by counting the number of atoms per unit volume.

The simulations predict a compression wave of ~7% propagating through the BCC crystal before the transformation to an HCP-like structure. For the compressive mechanism, no rotation of the crystal lattice would be expected even with uniaxial compression. For the slip/shear mechanism, in contrast, we would expect the rotation of the lattice to decrease from 5% to 3.5%, in order to form perfect hexagons following uniaxial compression. A rotation in real space is manifested in reciprocal space as a rotation in the pattern of peaks. In Fig. 3.2.4, we show an expanded view of the simulated $\left[2\bar{1}\bar{1}0\right]_{HCP}/(002)_{BCC}$ spot in reciprocal space. Also shown on the plot are dashed lines oriented 2° and 5° relative to the $[001]_{BCC}$ axis. With two possible directions that the rotation can occur, we would expect to see the HCP feature composed of two spots, each slightly shifted off the axis. However, the spot is a single diffuse spot (of order 1° FWHM) centered along the $[001]_{BCC}$ axis. We conclude from the simulations that the $\alpha-\varepsilon$ transition is predicted to occur by the compressive mechanism.

In Situ, Real-Time Diffraction Measurements During the Shock: The experiments described here were performed using the OMEGA [Boehly 1995], Janus, and Vulcan [Danson 1993] lasers. Melt-grown single-crystal iron samples with a purity of 99.94% were polished to a thickness of ~250 μm with the surfaces aligned along the [001] direction. These samples were shock loaded by direct laser irradiation at 10^{10} to 10^{12} W/cm^2 using 2 to 6 ns constant intensity laser pulses with a laser focal spot size of 2 to 3 mm in diameter and probed with 1.85 angstrom iron K-shell x-rays. Due to absorption in these thick samples, x-rays were diffracted from the shocked-side of the iron crystal in reflection geometry—which we refer to as the Bragg geometry. Experiments were also conducted using 10 μm thick single-crystal samples of iron. For these thinner samples it was also possible to perform diffraction in transmission geometry, which we refer to as Laue geometry. Due to the divergence of the x-rays and the large angle which the crystal subtends to the X-ray source, the X-rays are simultaneously collected from many different lattice planes in the crystal. Two wide angle multiple film packs covering a total of nearly 2π steradians recorded the diffracted signal in both the Bragg and Laue geometries.

A typical diffraction pattern below the $\alpha-\varepsilon$ transition is shown in Fig. 3.2.5a from both the shocked and unshocked BCC lattice at a pressure of 5.4 GPa. In contrast, Fig. 3.2.5b shows data for a pressure of 26 GPa above the $\alpha-\varepsilon$ transition. In this latter case, we note that the $(002)_{BCC}$ plane splits into three components—the first corresponding to diffraction from unshocked

BCC, the second to shock-compressed BCC, and the third to a further degree of compression which we have attributed to the HCP phase, as discussed next.

The Transformation Mechanism: The experimental data analysis supports the conclusion that the high pressure ε phase is HCP and that it is polycrystalline with two preferentially ordered variants highly aligned relative to the original crystal. Out of the list of possible transformation mechanisms from the BCC to HCP structure that are consistent with static experiments [Wang 1998], only the two candidate pathways discussed previously are reasonably consistent with the number of observed variants and rotation of the lattice. We now contrast these two pathways.

Due to the degeneracy of the shift along the $(110)_{BCC}$ family of planes, there are 4 variants of the rotation of the $\left[2\bar{1}\bar{1}0\right]$ plane. The experimental Laue diffraction has shown that the transformed HCP crystal is polycrystalline suggesting that, if the slip/shear mechanism is responsible for the transition, then all four rotations would have occurred. We compare the data with an overlay of the 4 rotations assuming a single compression. As discussed earlier, a rotation of 3.5° would still be required by the slip/shear mechanism to form a hexagonal structure when the BCC crystal is uniaxially compressed by ~7%. Figure 3.2.6 shows line outs from the data with overlays of calculated lineshape, assuming all four degenerate lattice rotations exist. The arrows denote the center position of the diffraction lines. The simulated line outs are broadened and scaled to obtain a best fit with the data. It is apparent that a rotation larger then 2° would not be consistent with our data. This small rotation appears to rule out the slip/shear mechanism, even taking into account an imperfect hexagonal structure upon transformation. Thus we conclude that the experimentally measured pathway is consistent with only the compressive mechanism of those listed by Wang et al. and as predicted by the MD simulations.

These results represent one of the first detailed studies of the atomistic dynamics of a shock-induced transformation. We have been able to clearly identify the high-pressure crystallographic structures as well as the probable transformation pathways for atomistic motion. For the first time, we have demonstrated the existence of variants in the high-pressure phase, vital information predicted in MD simulations but that had not been previously observed in recovery experiments. In future work, we will strive to study transformation timescales through combined simulation and experiments.

4 Future Work

4.1 Dynamic melt: simulation and experiment

The kinetics of dynamically driven phase transitions, specifically melt, has been an important topic of experimental and theoretical investigation for several decades. Few empirical models have attempted to explain the processes occurring at the atomic level in materials shock driven to a Hugoniot state beyond the solid-liquid phase boundary [Ross 1969, Jin 2001]. Kinetics models based on a simple picture of nucleation and growth, such as the Johnson-Mehl-Avrami-Kolmogorov (JMAK) [Avrami 1939] model, have been employed to describe a variety of materials, but determination of the rate with which the melt phase grows is based on assumptions regarding the homogeneous or heterogeneous nature of the nucleation rate. As such, there could be a significant difference between materials of polycrystalline or single crystal structure. In the former, the grain boundaries may play the primary role in the kinetics of the melt transition, whereas in the latter, dislocations and crystal orientation may be the determining factor of the transition kinetics. Lastly, the loading history of the sample under investigation, namely the shock pressure duration and amplitude, is critical for the transition kinetics and final microstructure.

Combining results of dynamic compression experiments with large scale MD simulations is beginning to provide knowledge on the non-equilibrium processes occurring during ns-ps time-scales leading to melt. An example of simulated shock-induced melt results in single crystal Cu is presented here (figure 4.1.1), where the behavior of the [100] orientated crystal shocked to 300 GPa and T=6000K is shown [Bringa 2004]. The material exhibits melt within nanometers of the shock front, corresponding to a time-scale of a few ps. A plot of the calculated scattering function S(q) depicted in Fig. 4.1.2 from which information about the interatomic spacing in the liquid Cu can be extracted from the series of maxima.

Coupling MD results to experimental observables requires a dynamic technique capable of revealing transient structural information with ps-ns temporal resolution. Only recently have dynamic x-ray diffraction techniques managed to demonstrate such capability. Specifically, we have developed a novel cylindrical pinhole powder camera (CPPC) suitable for laser-based x-ray backlighting and shock wave generation that has successfully captured signal from polycrystalline and amorphous materials [Hawreliak 2007].

The camera consists of a cylindrical detector arrangement with a point x-ray source of He-like α or K-α radiation produced at the entrance of the camera along the cylinder axis as shown in Fig. 4.1.3. Samples are interrogated by the quasi-collimated x-ray beam obtained by a suitable pinhole arrangement. Diffracted x-rays reach the detector, consisting of image plates positioned around the cylinder walls, in both transmission and reflection. Information is recorded in the azimuthal angle direction ϕ and the scattering angle 2θ, thus making the instrument capable of a variety of material property measurements under shock conditions including texture as well as phase transitions. Proof of principle experiments demonstrating the camera's ability in measuring amorphous signals, such as those expected from shock-melted samples, have been successfully carried out. Fig. 4.1.4 shows x-ray diffraction from the surrogate amorphous material Metglas [$Ni_{55}Fe_{27}Co_{15}Si_{1.6}Al_{1.4}$], where peak positions and widths corresponding to the He-like Fe x-ray source were observed.

With feasibility demonstrated, we plan to implement this diffraction geometry under dynamic conditions to record the melt signature from a variety of materials. Of great interest will be the connection of our MD simulation results in shock-melted Cu with corresponding experiments, although the required shock pressure of >200 GPa may present a challenge. Additionally, bounding information on the melt kinetics may be provided by a simple pump-probe experiment where the relative timing of the x-ray source and shock wave is varied, perhaps to as fast as ~fs at new generation facilities such as LCLS. Such future investigations should offer a glimpse into the dynamics and kinetics of ultrafast melt phenomena via a multi-faceted theoretical and experimental effort coupling MD and potentially hydrocode simulations to dynamic diffraction techniques such as the CPPC described above.

4.2 Damage: In Situ Void Nucleation and Growth

The non-equilibrium nucleation of phase transformations and submicron porosity behind the shock wave result in a microscopically heterogeneous material. When release waves interact, the metal may be driven into tension leading to the nucleation and growth of voids from these heterogeneities. Small angle x-ray scattering (SAXS), which arises due to scattering from electron density fluctuations, is particularly sensitive to the abrupt change in electron density accompanying voids and thus is a powerful tool to follow the evolution of this process during shock compression. We discuss here our effort aimed at conducting real-time, in situ void studies during the shock release process.

As mentioned earlier, shock wave loading is accompanied by considerable defect production during both the compression and unloading portions of the process. Defects and other microstructure (e.g. grain boundaries, second phase regions) may act as nucleation sites for the formation of voids. These voids can grow and coalesce under tension, resulting in material failure as exemplified in the micrograph of a shock recovered sample shown in Fig. 4.2.1. The time to failure can be fast from ~sub-ns to ~μs, depending upon the drive conditions in the experiment. The entirety of this process is termed spall.

Most experimental observations of the spall process have been generated using two methods: velocimetry and recovery. These types of measurements, while valuable, are inherently limited. Velocimetry measurements are continuum measurements that cannot identify or provide direct insight into the underlying processes. Similarly, shock recovered samples [Gray, 1993] have proven essential in identifying microscopic flaws and residual void distributions, but they are limited by the difficulty of or uncertainty in arresting the damage evolution during high strain-rate dynamic loading. In situ, temporally resolved studies offer the opportunity to potentially answer key questions in the nucleation, early void growth and final void linkage regimes.

The SAXS technique is well-established and has been applied to problems ranging from biology to materials science. In its simplest form, the SAXS scattered intensity is the square of the Fourier Transform of the scattering length density [Roe 2000, Glatter 1982]. In the dilute approximation, scattering is only a function of the form factor, or size and shape of the particles or voids [SAXS comment]. Although a given electron density distribution gives a unique scattering intensity profile, the inversion is not unique and requires model assumptions about microstructure.

To make our initial assessment, we performed SAXS experiments using incipiently spalled Ti samples recovered from laser shock experiments. The resulting static small-angle scattering data is shown in Fig. 4.2.2 [APS comment, Ilavsky 2002, Ilavsky 2004]. The maximum entropy method, implemented in the "Irena" package for SAXS data analysis, was used to determine scatterer size distributions [Ilavsky 2005]. For this study, the voids were modeled using a form factor for spheres, and a maximum entropy algorithm was employed to calculate size distributions of the voids [Ilavsky 2005]. This iterative, linear inversion method, which does not require an *a priori* guess as to the shape of the distribution, converges to a unique distribution of sizes for a given form factor by maximizing the configurational entropy subject to fitting the measured scattering profile [Ilavsky 2005, Potton 1988a, Potton 1998b]].

We believe that time dependent SAXS is an ideal technique to quantify the nucleation and growth of sub-micron voids under shock compression. To make our initial assessment, we performed SAXS experiments at the Advanced Photon Source (APS), whose single bunch mode capability allows the isolation of signal from only one bunch for time dependent x-ray experiments. To further increase the x-ray fluence, the APS beamline was operated with a ~ 4% energy spread around the characteristic energy, which increases the fluence by a factor of 10 yet does significantly degrade our desired angular resolution.

To demonstrate the ability to perform dynamic SAXS measurements, we used the unique time-resolved SAXS detector built by Dr. Jan Hessler at APS [De Lurgio 2005]. Small angle scattering signals were acquired through the use of a specialized solid state CCD that has ring shaped pixels that assume circumferential symmetry of the scattering signals but markedly increase the collected signal. The detector can record a single 120 ps x-ray pulse with a temporal resolution of 300 ns, which is sufficient to gate against subsequent x-ray pulses. We show data in Fig. 4.2.3 from a single pulse measurement of a Ti foil to demonstrate that time resolved SAXS measurements are feasible.

In Fig. 4.2.4, we show an MD simulation of spall fracture in dynamically compressed single crystal copper loaded to ~90 GPa in 60 ps and then released and along with its corresponding calculated SAXS signal. During the loading process, stacking faults and dislocations are formed to relieve the flow stress. MD simulations can identify the primary mechanisms for nucleation, growth and coalescence of voids, and determine Burgers vectors and habit planes of the dislocations observed. Such results can be parametrized and transitioned to higher-level statistical models such as dislocation dynamics or level-set coalescence calculations. Simulating the x-ray scattering using a Fourier transform of the MD simulation output shows the resolution required to measure the voids at this early stage of material failure.

Our combined experiment and simulation studies strongly indicate that single shot SAXS has the ability to provide relevant and valuable void formation data in dynamically loaded metals. With the goal of developing this in situ approach, we have demonstrated several key intermediate steps. We have shown, through shock-recovered measurements, that SAXS can provide valuable information about size distribution of microvoids. We have established that time resolved measurements at a third generation x-ray source, such as the APS, can potentially enable such measurements under shock conditions. These static data are showing direct evidence of structure in shock recovered samples at length scales less that 1 μm. In parallel, we have simulated the growth of voids during spallation by using large scale MD simulations and then calculating the experimental observables. Being able to quantify the temporal evolution of these voids under shock conditions by using both experiment and simulation would be exceedingly valuable in ultimately understanding the processes controlling void phenomenology.

Conclusion

This ongoing work couples together large-scale simulations that model the response of materials at the atomistic level to state-of-the-art experiments in order to address the multi-scale problem of building predictive models of material response under highly dynamic environments. Applying these capabilities to the shock process, we have investigated and obtained interesting insight into the 1D to 3D transition and the generation and motion of dislocations. While laser-based experiment and simulation agree very well for iron, the discrepant results of short timescale laser-based experiments and long timescale gas gun experiments have raised intriguing questions as to the processes that affect the kinetics of the plastic response. Using in-situ x-ray diffraction, we have studied the shock-induced high pressure phase of iron and found both the pathway and structure to be in good agreement with MD simulations. In addition, we are developing techniques that can be used both to diagnose material melting under dynamic loading and that can be used to address polycrystalline solids where grain boundaries and the interaction of differently oriented crystallites introduce fascinating and complicated phenomena. And finally, we are investigating void formation and material failure during the dynamic tensile stress conditions often generated under shock release. These efforts are poised to provide a more complete picture of the shock response of crystalline materials than has been previously possible.

This work was funded by the Laboratory Directed Research and Development Program at LLNL under project tracking code 06-SI-004 and under the auspices of the U.S. Department of Energy by Lawrence Livermore National Laboratory under Contract DE-AC52-07NA27344. Work at the Advanced Photon Source was supported by the U.S. Department of Energy, Office of Science, Office of Basic Energy Sciences, under Contract No. DE-AC02-06CH11357. The authors would like to thank the staff at the Vulcan Laser Facility at the Rutherford Appleton Laboratory, the Janus laser at Lawrence Livermore National Laboratory, and the University of Rochester Laboratory for Laser Energetics under the NLUF grants program. MT acknowledges the Secretaría de Estado de Educación y Universidades of the Government of Spain for a postdoctoral fellowship and the MEC for partial support through grant MAT2006-13548-C02-01.

References

[APS comment] The Ultra small angle x-ray scattering (USAXS) data were acquired using the beam line 32-ID at the Advanced Photon Source, Argonne National Laboratory, Argonne, Illinois, U.S.A. The endstation consists of a Bonse-Hart camera, which can measure scattering vectors (*q*) from about 0.0001 to 10 Å^{-1}. The monochromator was positioned at about 11 keV (1.13 Å). Data were processed using the codes developed for use on this USAXS instrument, and included absolute scattering intensity calibration and slit desmearing.

[Asay 1997] Asay JR. "The use of shock-structure methods for evaluating high-pressure material properties". International Journal of Impact Engineering 1997;20(1-5):27-61.

[Avrami 1939] Avrami M. "Kinetics of phase change I - General theory". J Chem Phys 1939;7(12):1103-1112.

[Bancroft 1956] Bancroft D, Peterson EL, Minshall S. "Polymorphism of Iron at High Pressure". Journal of Applied Physics 1956;27(3):291-298.

[Boehly 1995] Boehly TR, Craxton RS, Hinterman TH, Kelly JH, Kessler TJ, Kumpan SA, Letzring SA, McCrory RL, Morse SFB, Seka W, Skupsky S, Soures JM, Verdon CP. The upgrade to the OMEGA laser system. Proceedings of the tenth topical conference on high temperature plasma diagnostics, Vol. 66 Rochester, New York: AIP, 1995, p. 508.

[Boettger 1997] Boettger JC, Wallace DC. "Metastability and dynamics of the shock-induced phase transition in iron". Physical Review B 1997;55(5):2840-2849.

[Boustie 1996] Boustie M, De Resseguier T, Hallouin M, Migault A, Romain JP, Zagouri D. "Some applications of laser-induced shocks on the dynamic behavior of materials". Laser and particle beams(Print) 1996;14(2):225-235.

[Bringa 2004] Bringa EM, Cazamias JU, Erhart P, Stolken J, Tanushev N, Wirth BD, Rudd RE, Caturla MJ. "Atomistic shock Hugoniot simulation of single-crystal copper". Journal of Applied Physics 2004;96(7):3793-3799.

[Bringa 2005] Bringa EM, Caro A, Wang YM, Victoria M, McNaney JM, Remington BA, Smith RF, Torralba BR, Van Swygenhoven H. "Ultrahigh strength in nanocrystalline materials under shock loading". Science 2005;309:1838-1841.

[Bringa 2006] Bringa EM, Rosolankova K, Rudd RE, Remington BA, Wark JS, Duchaineau M, Kalantar, DH, Hawreliak J, Belak J. "Shock deformation of face-centred cubic metals on subnanosecond timescales". Nature Materials 2006;5:805-809.

[Bundy 1996] Bundy FP, Bassett WA, Weathers MS, Hemley RJ, Mao HU, Goncharov AF. "The pressure-temperature phase and transformation diagram for carbon; updated through 1994". Carbon 1996;34(2):141-153.

[Burgers 1934] Burgers WG. "On the process of transition of the cubic-body-centered modification into the hexagonal-close-packed modification of zirconium". Physica 1934;1(7-12):561.

[Colvin 2003] Colvin JD, Ault ER, King WE, Zimmerman IH. "Computational model for a low-temperature laser-plasma driver for shock-processing of metals and comparison to experimental data". Physics of Plasmas 2003;10:2940.

[Cornacchia 2004] Cornacchia M, Arthur J, Bane K, Bolton P, Carr R, Decker FJ, Emma P, Galayda J, Hastings J, Hodgson K, Huang Z, Lindau I, Nuhn HD, Paterson JM, Pellegrini C, Reiche S, Schlarb H, Stöhr J, Stupakov G, Walz D, Winick H. "Future Possibilities of the Linac Coherent Light Source". logo 2004;11(Part 3):227-238.

[d'Almeida 2000] d'Almeida T, Gupta YM. "Real-time X-ray diffraction measurements of the phase transition in KCl shocked along [100]". Phys Rev Lett 2000;85:330-333.

[Danson 1993] Danson CN, Barzanti LJ, Chang Z, Damerell AE, Edwards CB, Hancock S, Hutchinson MHR, Key MH, Luan S, Mahadeo RR. "High contrast multi-terawatt pulse generation using chirped pulse amplification on the VULCAN laser facility". Optics Communications 1993;103(5-6):392-397.

[Davidson 2002] Davidson RC, Arnett D, Dahlburg J, Dimotakis P, Dubin D, Gabrielse G, Hammer D, Katsouleas T, Kruer W, Lovelace R. "Frontiers in High Energy Density Physics: The X-Games of Contemporary Science". Frontiers 2002.

[De Lurgio 2005]De Lurgio PM, Hessler JP, Weizeorick JT, Kreps AS, Molitsky MJ, Naday I, Drake GR, Jennings G. "A New Detector for Time-Resolved Small-Angle X-Ray Scattering Studies". Nuclear Science Symposium 2005;2:1215-1222.

[Duff 1957] Duff RE, Minshall FS. "Investigation of a Shock-Induced Transition in Bismuth". Physical Review 1957;108(5):1207-1212.

[Edwards 2004] Edwards J, Lorenz KT, Remington BA, Pollaine S, Colvin J, Braun D, Lasinski BF, Reisman D, McNaney JM, Greenough JA, Wallace R, Louis H, Kalantar D. "Laser-driven plasma loader for shockless compression and acceleration of samples in the solid state". Physical Review Letters 2004;92(7):075002.

[Glatter 1982] Glatter O, Kratky O, editors. Small Angle X-ray Scattering. London: Academic Press Inc., 1982.

[Gray 1993] Gray III GT. "Influence of shock-wave deformation on the structure/property behavior of materials". High Pressure Shock Compression of Solids, JR Asay and M Shahinpoor, eds, Springer-Verlag;1993:187-215.

[Hawreliak 2006] Hawreliak J, Colvin JD, Eggert JH, Kalantar DH, Lorenzana HE, Stolken JS, Davies HM, Germann TC, Holian BL, Kadau K, Lomdahl PS, Higginbotham A, Rosolankova K, Sheppard J, Wark JS. "Analysis of the x-ray diffraction signal for the alpha-epsilon transition in shock-compressed iron: Simulation and experiment". Physical Review B (Condensed Matter and Materials Physics) 2006;74(18):184107.

[Hawreliak 2007] Hawreliak J, Lorenzana HE, Remington BA, Lukezic S, Wark JS. "Nanosecond x-Ray diffraction from polycrystalline and amorphous materials in a pinhole camera geometry suitable for laser shock compression experiments". Rev Sci Instrum 2007;78(8):-.

[Holian 1998] Holian BL, Lomdahl PS. "Plasticity induced by shock waves in nonequilibrium molecular-dynamics simulations". Science 1998;280(5372):2085-2088.

[Ilavsky 2002] Ilavsky J, Allen AJ, Long GG, Jemian PR. "Effective pinhole-collimated ultrasmall-angle x-ray scattering instrument for measuring anisotropic microstructures". Review of Scientific Instruments 2002;73:1660.

[Ilavsky 2004] Ilavsky J, Jemian P, Allen AJ, Long GG. "Versatile USAXS (Bonse-Hart) Facility for Advanced Materials Research". AIP Conference Proceedings 2004;705:510.

[Ilavsky 2005] Ilavsky J, Jemian PR. Irena and Indra SAXS data analysis macros, including Maximum Entropy. 2005.

[Jemian 1990] Jemian PR. Characterization of Steels by Anomalous Small-angle X-ray Scattering. In: Materials Science and Engineering Evanston, IL: Northwestern University, 1990, p. 222.

[Jin 2001] Jin ZH, Gumbsch P, Lu K, Ma E. "Melting Mechanisms at the Limit of Superheating". Phys Rev Lett 2001;87(5).

[Johnson 1972] Johnson Q, Mitchell AC. "First X-Ray Diffraction Evidence for a Phase Transition during Shock-Wave Compression". Physical Review Letters 1972;29(20):1369.

[Kadau 2002] Kadau K, Germann TC, Lomdahl PS, Holian BL. "Microscopic view of structural phase transitions induced by shock waves". Science 2002;296(5573):1681-1684.

[Kalantar 1999] Kalantar DH, Chandler EA, Colvin JD, Lee R, Remington BA, Weber SV, Wiley LG, Hauer A, Wark JS, Loveridge A, Failor BH, Meyers MA, Ravichandran G. "Transient x-ray diffraction used to diagnose shock compressed Si crystals on the Nova Laser". Review of Scientific Instruments 1999;70:629-632.

[Kalantar 2000] Kalantar DH, Remington BA, Colvin JD, Mikaelian KO, Weber SV, Wiley LG, Wark JS, Loveridge A, Allen AM, Hauer AA. "Solid-state experiments at high pressure and strain rate". Physics of Plasmas 2000;7:1999.

[Kalantar 2003] Kalantar DH, Bringa E, Caturla M, Colvin J, Lorenz KT, Kumar M, Stolken J, Allen AM, Rosolankova K, Wark JS, Meyers MA, Schneider M, Boehly TR. "Multiple film plane diagnostic for shocked lattice measurements (invited)". Review of Scientific Instruments 2003;74:1929-1934.

[Kalantar 2005] Kalantar DH, Belak JF, Collins GW, Colvin JD, Davies HM, Eggert JH, Germann TC, Hawreliak J, Holian BL, Kadau K, Lomdahl PS, Lorenzana HE, Meyers MA, Rosolankova K, Schneider MS, Sheppard J, Stolken JS, Wark JS. "Direct Observation of the alpha-epsilon Transition in Shock-Compressed Iron via Nanosecond X-Ray Diffraction". Phys Rev Lett 2005;95(7):075502.

[Kim 2005] Kim KJ, Mills DM. "Workshop Generation and Use of Short X-ray Pulses at APS". Advanced Photon Source, Argonne National Laboratory 2005.

[Kozlov 2005] Kozlov EA, Telichko IV, Gorbachev DM, Pankratov DG, Dobromyslov AV, Taluts NI. "The metastability and incompleteness of the alpha-epsilon phase transformation in unalloyed iron loading pulses: Specific features under the effect of threshold of the deformation behavior and structure of armco iron". Physics of Metals and Metallography 2005;99(3):300-313.

[Lindl 1995] Lindl J. "Development of the indirect-drive approach to inertial confinement fusion and the target physics basis for ignition and gain". Physics of Plasmas 1995;2(11):3933-4024.

[Lorenz 2005] Lorenz KT, Edwards MJ, Glendinning SG, Jankowski AF, McNaney J, Pollaine SM, Remington BA. "Accessing ultrahigh-pressure, quasi-isentropic states of matter". Physics of Plasmas 2005;12(5):056309.

[Loveridge-Smith 2001] Loveridge-Smith A, Allen A, Belak J, Boehly T, Hauer A, Holian B, Kalantar D, Kyrala G, Lee RW, Lomdahl P, Meyers MA, Paisley D, Pollaine S, Remington B, Swift DC, Weber S, Wark JS. "Anomalous elastic response of silicon to uniaxial shock compression on nanosecond time scales". Phys Rev Lett 2001;86(11):2349-2352.

[Mao 1967] Mao H, Bassett WA, Takahashi T. "Effect of Pressure on Crystal Structure and Lattice Parameters of Iron up to 300 kbar". Journal of Applied Physics 1967;38(1):272-276.

[Meyers 1994] Meyers MA, Meyers M. Dynamic Behavior of Materials. Wiley-IEEE, 1994.

[Meyers 2003] Meyers MA, Gregori F, Kad BK, Schneider MS, Kalantar DH, Remington BA, Ravichandran G, Boehly T, Wark JS. "Laser-induced shock compression of monocrystalline copper: characterization and analysis". Acta Materialia 2003;51(5):1211-1228.

[Ochi 2003] Ochi Y, Golovkin I, Mancini R, Uschmann I, Sunahara A, Nishimura H, Fujita K, Louis S, Nakai M, Shiraga H. "Temporal evolution of temperature and density profiles of a laser compressed core (invited)". Review of Scientific Instruments 2003;74:1683.

[Park 2008] Park HS, Maddox, BR, Giraldez, E, Hatchett, SP, Hudson, LT, Izumi, N, Key, MH, Le Pape, S, MacKinnon, AJ, MacPhee, AG, Patel, PK, Phillips, TW, Remington, BA, Seeley, JF, Tommasini, R, Town, R, Workman, J, and Brambrink, E. "High-Resolution 17-75 KeV Backlighters for High Energy Density Experiments". Physics of Plasmas 2008; 15: 072705.

[Phillion 1986] Phillion DW, Hailey CJ. "Brightness and Duration of X-Ray-Line Sources Irradiated with Intense 0.53-Mu-M Laser-Light at 60 and 120 Ps Pulse Width". Physical Review A 1986;34(6):4886-4896.

[Potton 1988a] Potton JA, Daniell GJ, Rainford BD. "A New Method for the Determination of Particle Size Distributions from Small-angle Neutron Scattering Measurements". J Appl Cryst 1988;21:891-897.

[Potton 1988b] Potton JA, Daniell GJ, Rainford BD. "Particle Size Distributions from SANS Data Using the Maximum Entropy Method". J Appl Cryst 1988;21:663-668.

[Preston 2002] Preston DL, Tonks DL, Wallace DC. "Model of plastic deformation for extreme loading conditions". Journal of Applied Physics 2002;93:211.

[Remington 2005] Remington BA, Cavallo RM, Edwards MJ, Ho DDM, Lasinski BF, Lorenz KT, Lorenzana HE, McNaney JM, Pollaine SM, Smith RF. "Accessing high pressure states relevant to core conditions in the giant planets". Astrophysics and Space Science 2005;298(1-2):235-240.

[Rigg 1998] Rigg PA, Gupta YM. "Real-time x-ray diffraction to examine elastic--plastic deformation in shocked lithium fluoride crystals". Appl Phys Lett 1998;73(12):1655-1657.

[Rigg 2003] Rigg PA, Gupta YM. "Time-resolved x-ray diffraction measurements and analysis to investigate shocked lithium fluoride crystals". Journal of Applied Physics 2003;93(6):3291-3298.

[Roe 2000] Roe RJ. Methods of X-ray and Neutron Scattering in Polymer Science. Oxford University Press, 2000.

[Romain 1986] Romain JP, Cottet F, Hallouin M, Fabbro R, Faral B, Pepin H. "Laser shock experiments at pressures above 100 Mbar". Physica, B+ C 1986;139:595-598.

[Rosolankova 2005] Rosolankova K. Picosecond X-ray Diffraction from Shock-Compressed Metals: Experiments and Computational Analysis of Molecular Dynamics Simulations In: Atomic and Laser Physics, Vol. D. Phil. Oxford: University of Oxford, 2005, p. 207.

[Rosolankova 2006] Rosolankova K, Wark JS, Bringa EM, Hawreliak J. "Measuring stacking fault densities in shock-compressed FCC crystals using in situ x-ray diffraction". Journal of Physics: Condensed Matter 2006;18(29):6749-6757.

[Ross 1969] Ross M. "Generalized Lindemann Melting Law". Physical Review 1969;184(1):233-242.

[SAXS Comment] In this approximation, and for a single population of scatterers, the scattering can be written in the following form [Ilavsky 2005, Jemian 1990]:

$$I(q) = |\Delta\rho|^2 \int_0^\infty |F(q,r)|^2 V^2(r) NP(r) dr$$

where $q = \frac{4\pi}{\lambda}\sin(\theta)$, λ is the wavelength of scattered radiation, θ is the scattering half, r is the size of the scattering particle, $\Delta\rho$ is the scattering contrast (related to the difference in electron density) between the minority and majority phases, $F(q,r)$ is the scattering form factor, $V(r)$ is the volume of the particle, N is the total number of particles, and $P(r)$ is the probability of having a minority phase particle of size r.

[Schneider 2004] Schneider MS, Kad BK, Gregori F, Kalantar D, Remington BA, Meyers MA. "Laser-induced shock compression of copper: Orientation and pressure decay effects". Metallurgical and Materials Transactions a-Physical Metallurgy and Materials Science 2004;35A(9):2633-2646.

[Smith 1958] Smith CS. "Metallographic studies of metals after explosive shock". Trans Metal Soc AIME 1958;212:574-589.

[Swift 2001] Swift DC, Ackland GJ, Hauer A, Kyrala GA. "First-principles equations of state for simulations of shock waves in silicon". Physical Review B 2001;6421(21):art. no.-214107.

[Wang 1998] Wang FM and Ingalls R. "Iron bcc-hcp transition: Local structure from x-ray absorption fine structure". Physical Review B 1998; 57(1): 5647-5654.

[Wark 1989] Wark JS, Whitlock RR, Hauer AA, Swain JE, Solone PJ. "Subnanosecond x-ray diffraction from laser-shocked crystals". Physical Review B 1989;40(8):5705-5714.

[Yamada 2000] Yamada K, Tanabe Y, Sawaoka AB. "Allotropes of carbon shock synthesized at pressures up to 15 GPa". Philosophical Magazine A 2000;80(8):1811-1828.

Figures

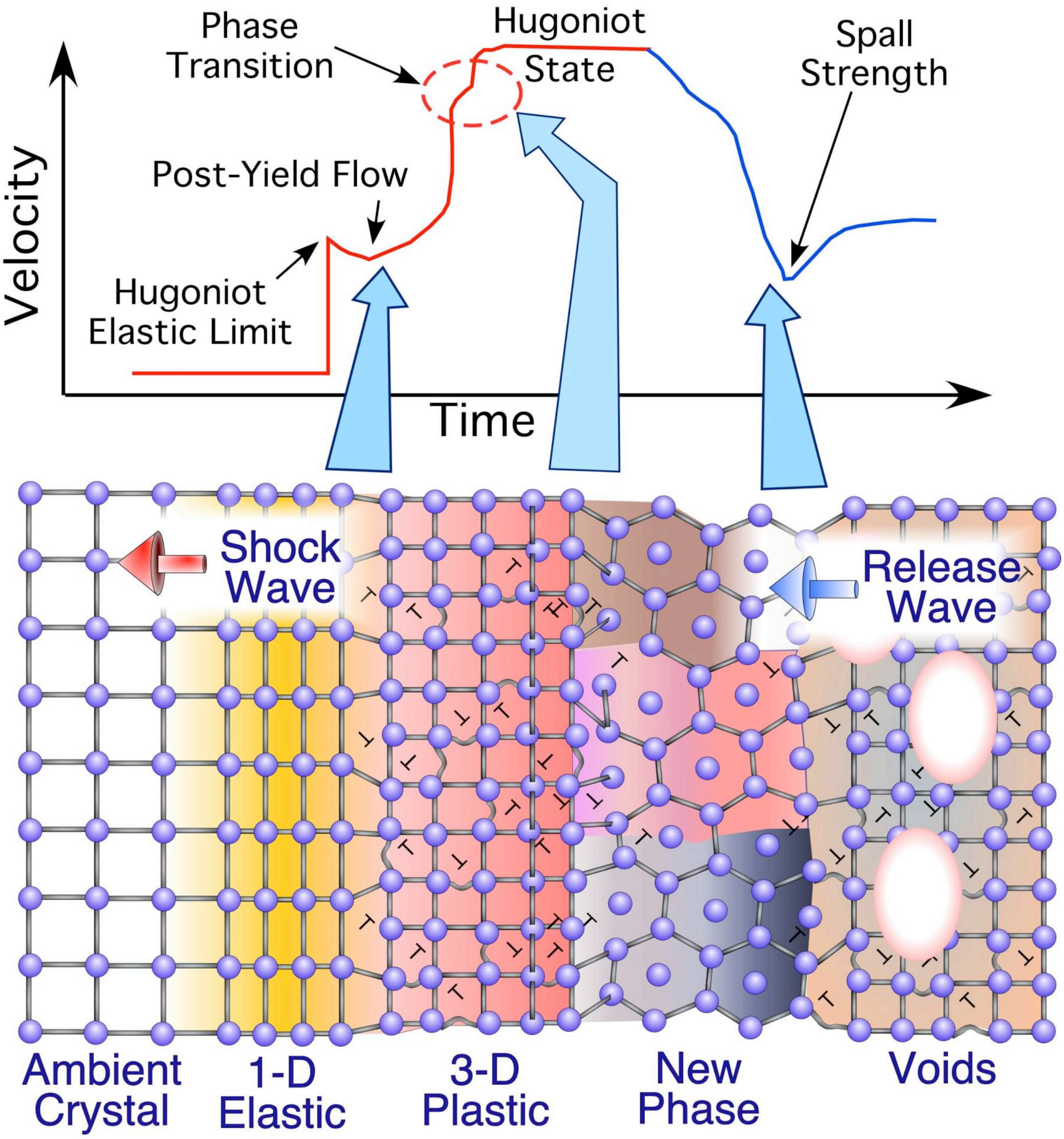
Phase
Transition
Hugoniot
State
Spall
Strength
Velocity
Post-Yield Flow
Hugoniot
Elastic Limit
Time
Shock
Wave
Release
Wave
Ambient
Crystal
1-D
Elastic
3-D
Plastic
New
Phase
Voids

Figure 1.1: A schematic diagram of a shocked crystalline solid, linking microstructural processes to the bulk behavior measured through conventional velocimetry. Material properties are typically inferred from the change in velocity at the surface of a target sample (top panel). The rearrangement of the atoms as the lattice relaxes plastically or undergoes a phase-transition alters the response of the material causing a change in surface velocity (bottom panel). While a change in slope indicates a change in material response, it does not provide any information on the microscopic lattice details.

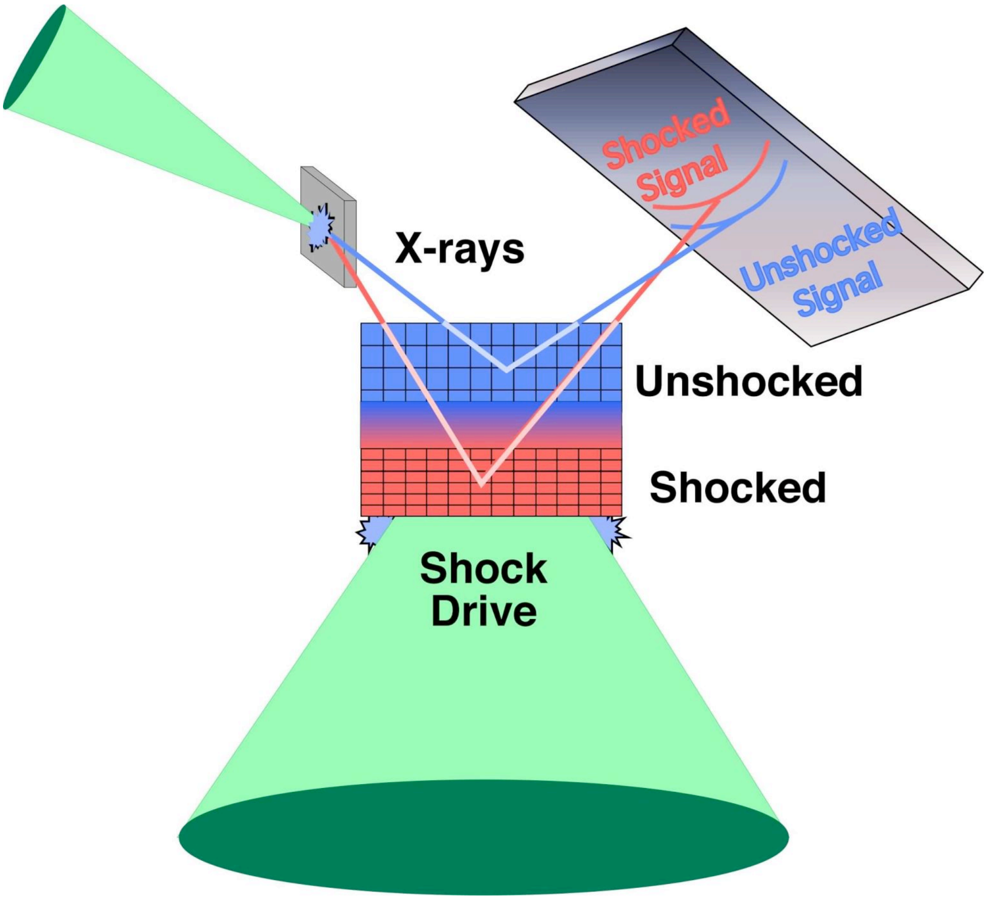
Shocked Signal
Unshocked Signal
X-rays
Unshocked
Shocked
Shock Drive

Figure 2.1: A schematic diagram of the laser-based in situ x-ray diffraction technique for shock-loaded single-crystal solids. A pulsed beam is used to generate ablative pressure on a surface of a sample. As the shock propagates, another beam irradiates a metal foil whose pulsed K-shell x-rays are used to probe the crystal. By setting the relative timing of the pump-probe experiment, it is possible to record both shocked and unshocked signal. Due to the geometry of the instrument, the diffraction from the lattice planes generate arcs whose curvature and position give insight into plane spacings and orientations.

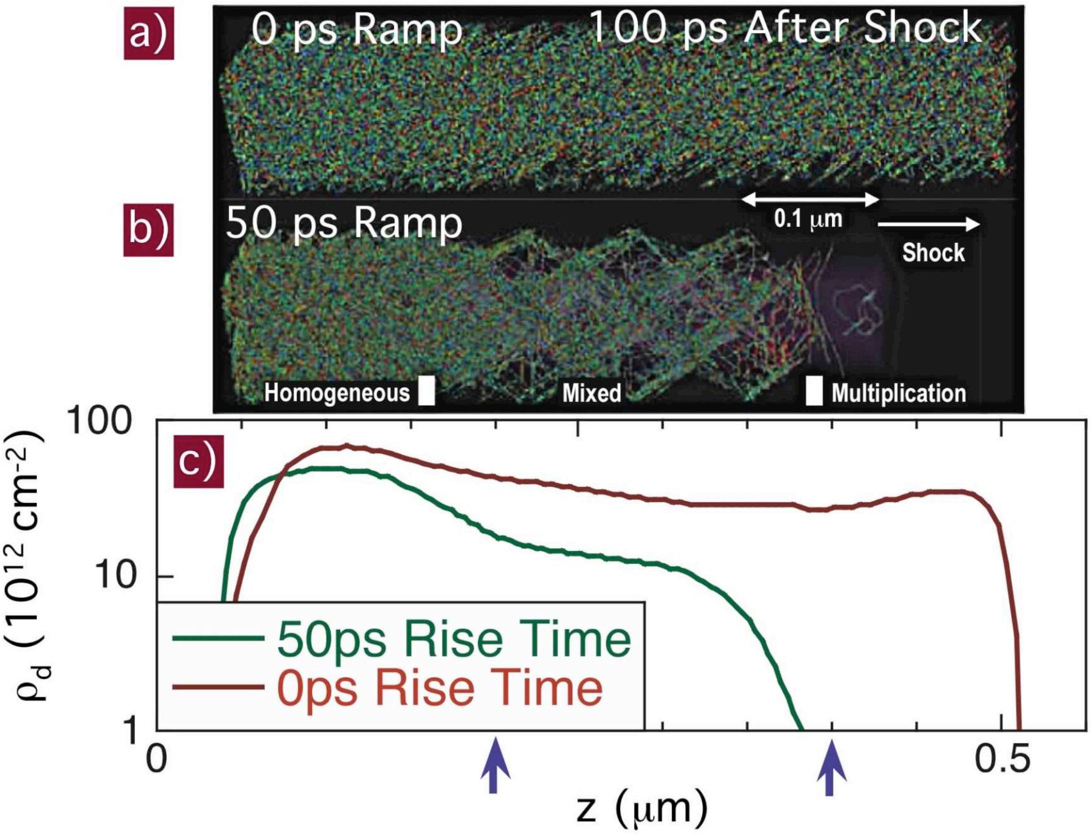

Figure 3.1.1: Contrast in the dislocation behaviors between the 0ps and 50ps ramp compressions in single-crystal copper. **a)** Shows a real space plot of the dislocation of atoms for a 0 ps rise time compression, 100 ps after the start of the shock. Dislocation activity appears to be fairly uniform and continuous throughout. **b)** A similar plot for the 50 ps rise time case with two distinguishable regions of dislocation activity, a multiplication and homogenous nucleation regimes with a transition region of mixed mechanisms. **c)** Dislocation density for both simulations. In both cases, the copper crystal included pre-existing dislocation sources located by the arrows. Marked differences in ρ_d occur in the vicinity of the initial dislocation sources. Peak particle speed is 0.75 km/s.

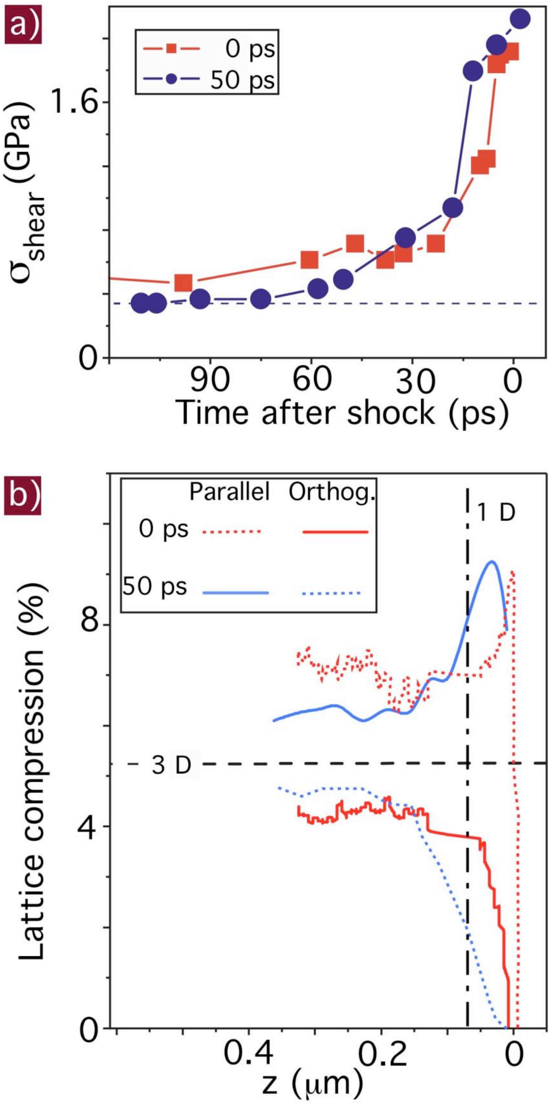

Figure 3.1.2: Plastic response of the 0ps and 50ps ramp compressions in single-crystal copper. **a**) Shear stress relaxation under loading conditions of 0 and 50 ps rise time. **b**) The corresponding lattice compression from simulated X-ray diffraction for lattice planes whose normals are parallel and orthogonal to the shock direction. The shock front is located at $z = 0$. The black vertical line is at the limit of previous simulations while the horizontal shows the hydrostatic limit of relaxation. The 'jitter' of the curve corresponds to the magnitude of the error in our simulations and the dependence on local structure.

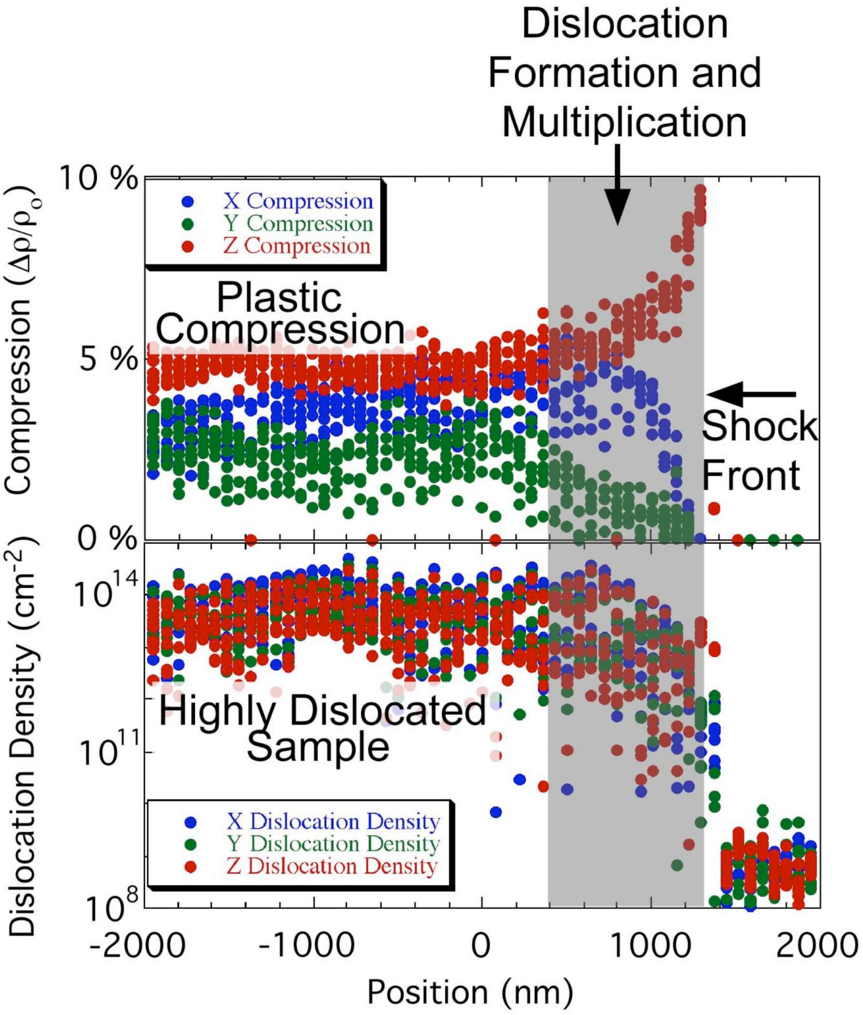

Figure 3.1.3: Using simulated x-ray diffraction, we estimate the stacking fault density and lattice compression with the same tools used to analyze experimental data. The agreement of these estimates with those determined from the MD simulations using other approaches serves to validate our tools. These results show that the loading close to the shock front is initially elastic, followed by a rapid formation of dislocations that eventually relieve the shear stress. Fluctuations are primarily due to statistical variations throughout the simulated sample. Directions X and Y are orthogonal and Z is parallel to the shock direction.

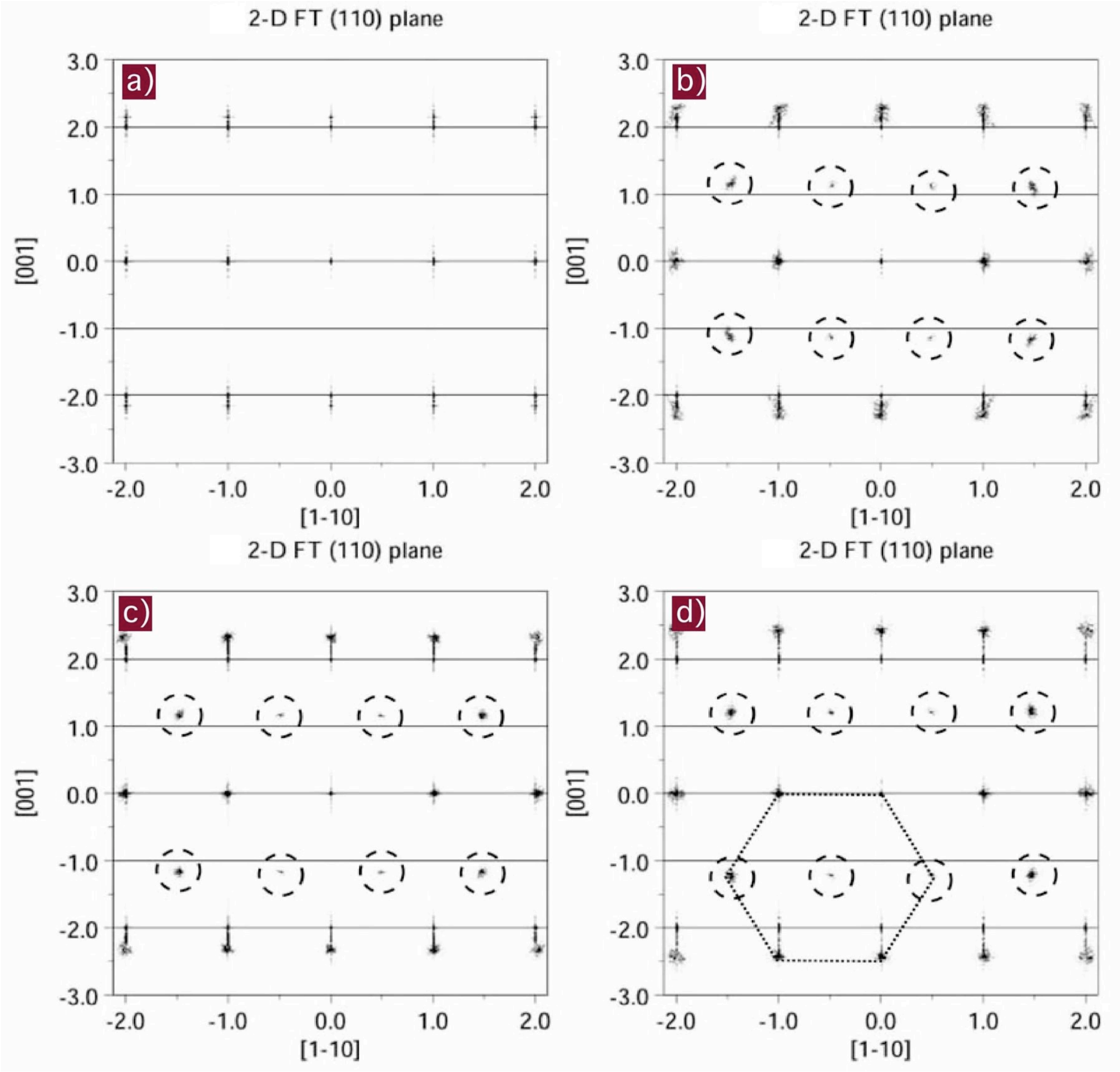

Figure 3.1.4: Simulated x-ray diffraction patterns from iron MD simulations performed in Kadau et al. 2002. The pressure corresponds to 15 GPa, 19.6 GPa, 28.8 GPa and 52.9 GPa for A, B, C and D, respectively. The discrete points correspond to different lattice planes. Uniaxial compression causes expansion along the [001] axis, while lattice relaxation results in expansion along the [110] axis. For these simulations, we do not see any change in lateral compression. At the α–ε transition, we see a doubling of the lattice, indicated by the appearance of the circled points. The k space units at $2/a_o$, where a_o is the lattice constant of the BCC unit cell.

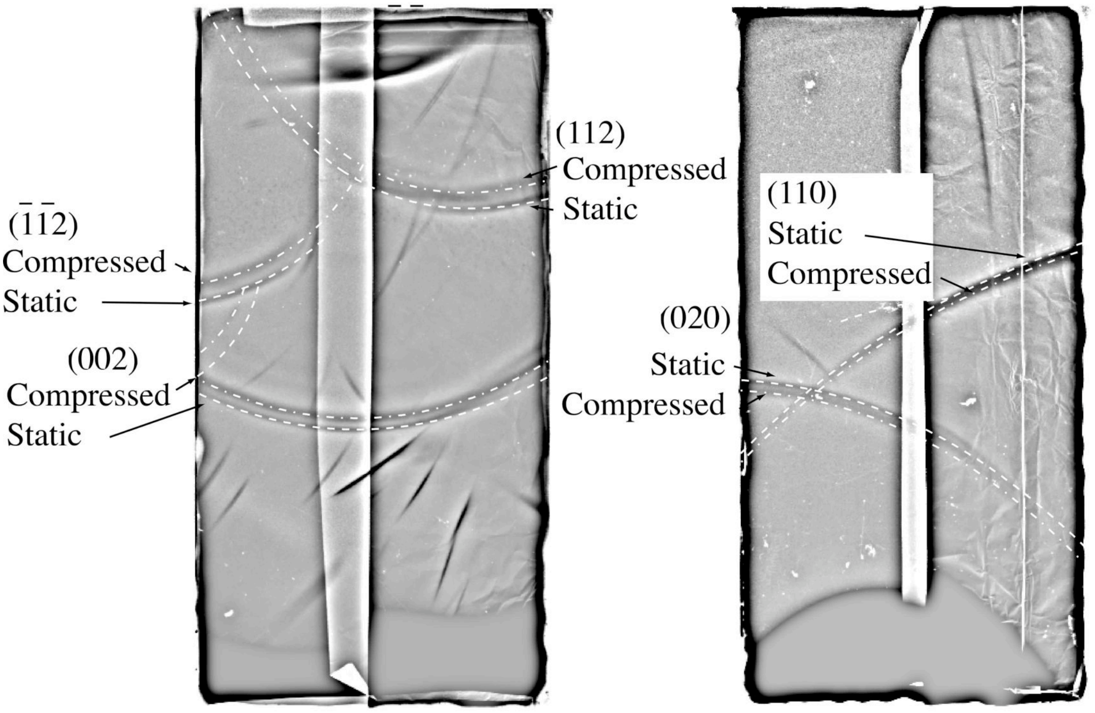

Figure 3.1.5: X-ray diffraction data from a vapor-deposited, single-crystal foil of iron shock-compressed to 11 GPa. In contrast to melt-grown single crystals, these vapor-deposited samples exhibited lattice relaxation after the shock that was faster than the nanosecond timescale of the measurements These experiments show that the initial defected state of the sample can strongly affect the lattice kinetics.

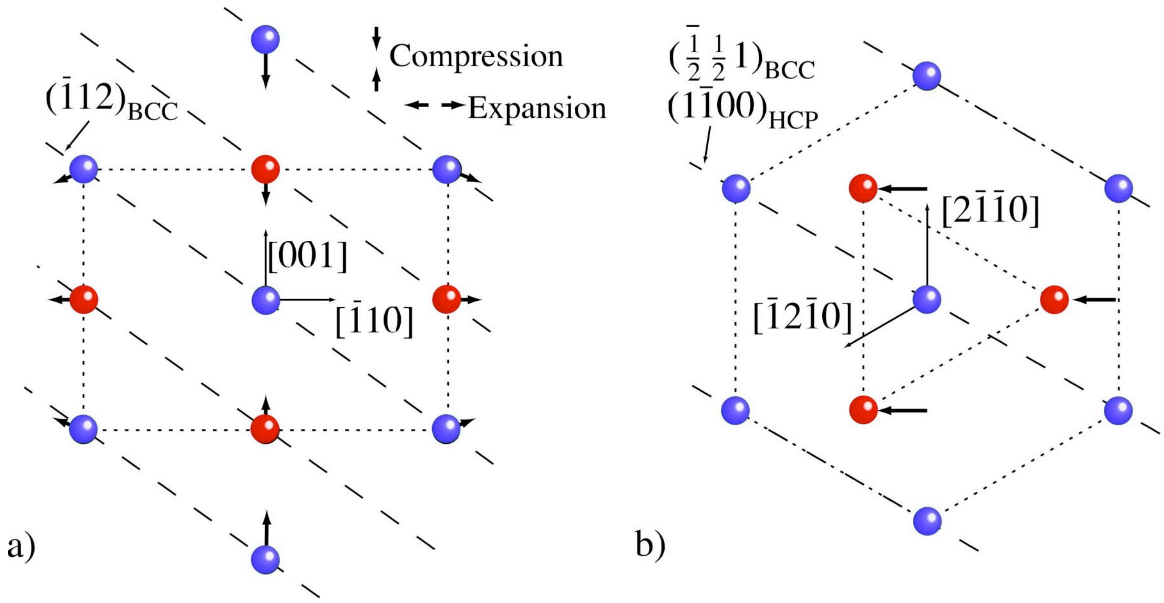
Compression
Expansion
$(\bar{1}12)_{BCC}$
[001]
$[\bar{1}10]$
a)
$(\frac{\bar{1}}{2}\frac{1}{2}1)_{BCC}$
$(1\bar{1}00)_{HCP}$
$[2\bar{1}\bar{1}0]$
$[\bar{1}2\bar{1}0]$
b)

Figure 3.2.1: Schematic diagram showing the transformation from BCC to HCP following the compression transition mechanism. The $(110)_{BCC}$ and $(0002)_{HCP}$ planes are in the plane of the paper. The blue and red circles denote atoms in the page and above the page, respectively. Arrows denote the direction of motion of the atoms. **a)** Defines the coordinate system in terms of the BCC lattice and has arrows showing the expansion/compression and dashed lines indicating the location of the $(\bar{1}12)_{BCC}$ planes. **b)** Defines the coordinate system for the HCP with arrows showing the shuffle of atoms with the $(1\bar{1}00)_{HCP}$ planes labeled which are equivalent to $(\bar{1}/_2\ 1/_2\ 1)_{BCC}$.

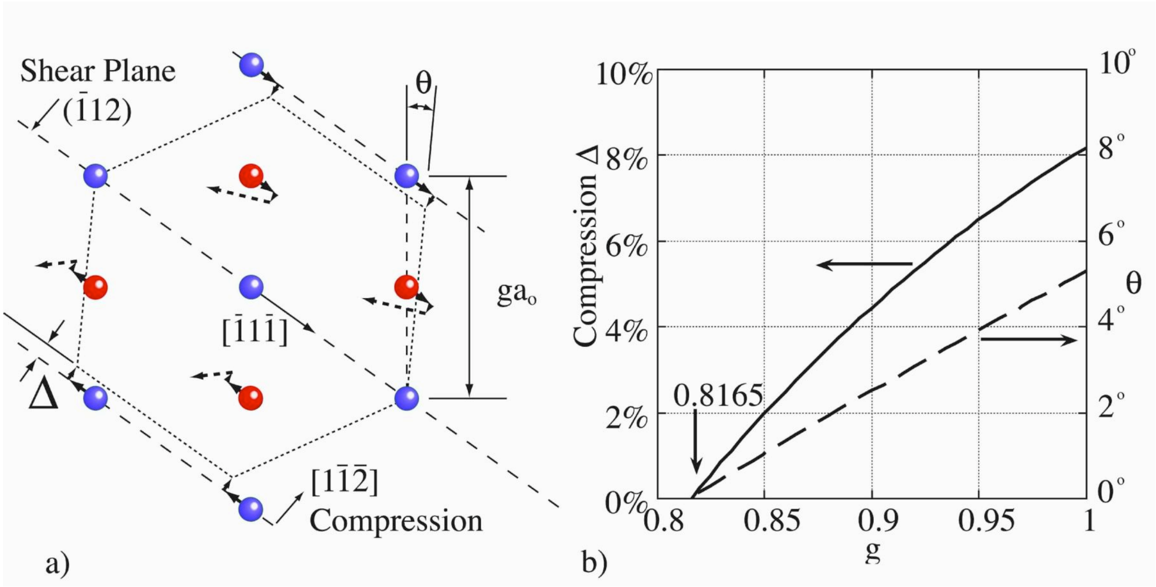
Shear Plane
$(\bar{1}12)$
θ
ga_o
$[\bar{1}1\bar{1}]$
Δ
$[1\bar{1}\bar{2}]$
Compression
a)
10%
8%
6%
4%
2%
0%
Compression Δ
0.8165
0.8
0.85
0.9
0.95
1
g
10°
8°
6°
4°
2°
0°
θ
b)

Figure 3.2.2: Transformation from BCC to HCP following the slip/shear mechanism. **a)** Schematic diagram showing the formation of hexagons in the $(110)_{BCC}$ plane. The blue and red circles denote atoms in the page and above the page, respectively. The $\left(\bar{1}1\bar{1}\right)_{BCC}$ shear plane, the $\left[1\bar{1}\bar{2}\right]_{BCC}$ direction, and the $\left[1\bar{1}\bar{2}\right]_{BCC}$ direction are labeled. The solid arrows denote the direction of the atomic motion due to the shear/compression. The dashed arrows represent the effective overall movement of the atoms when the crystal structure undergoes period doubling. **b**) Rotation of the HCP unit cell, θ, and required compression along $\left[1\bar{1}\bar{2}\right]_{BCC}$ to form the hexagon in the initial step as functions of the initial elastic compression, g, where g=1 for hydrostatic conditions.

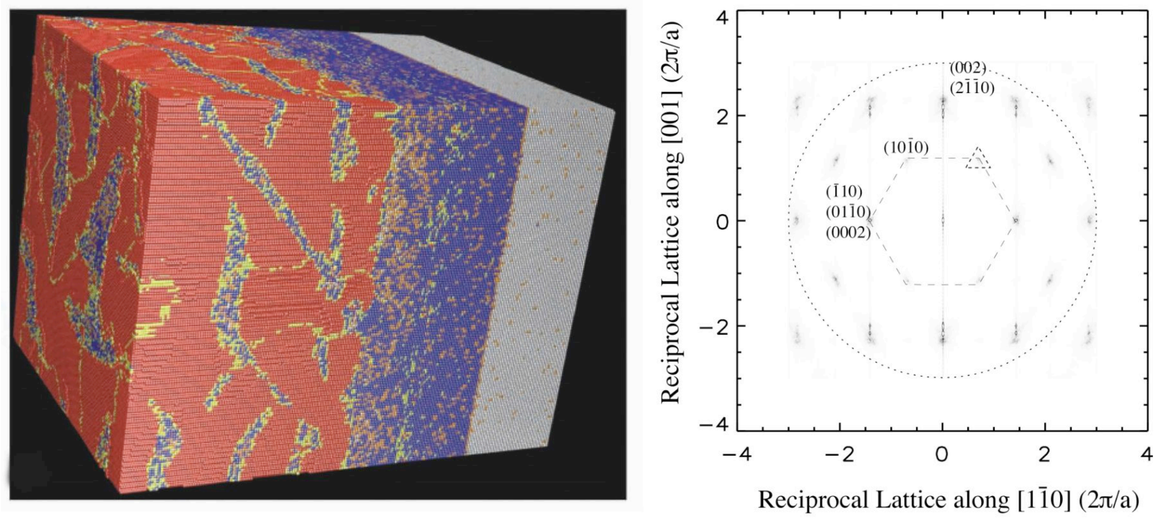

Figure 3.2.3: This figure schematically shows the method used in calculating the expected diffraction. The atomic positions from a select portion or entire MD simulation are Fourier transformed into reciprocal lattice space. The high intensity peaks represent diffraction planes in the crystal structure. The units are based on the inverse of the original cubic BCC cell. Three points are labeled with the plane indices. One point contains three labels to show that there is a BCC component and 2 degenerate HCP components. A dashed hexagon shows that the reciprocal lattice points are approaching a hexagonal symmetry. The dotted circle gives the limits that can be experimentally probed using 0.185 nm K-shell radiation from iron.

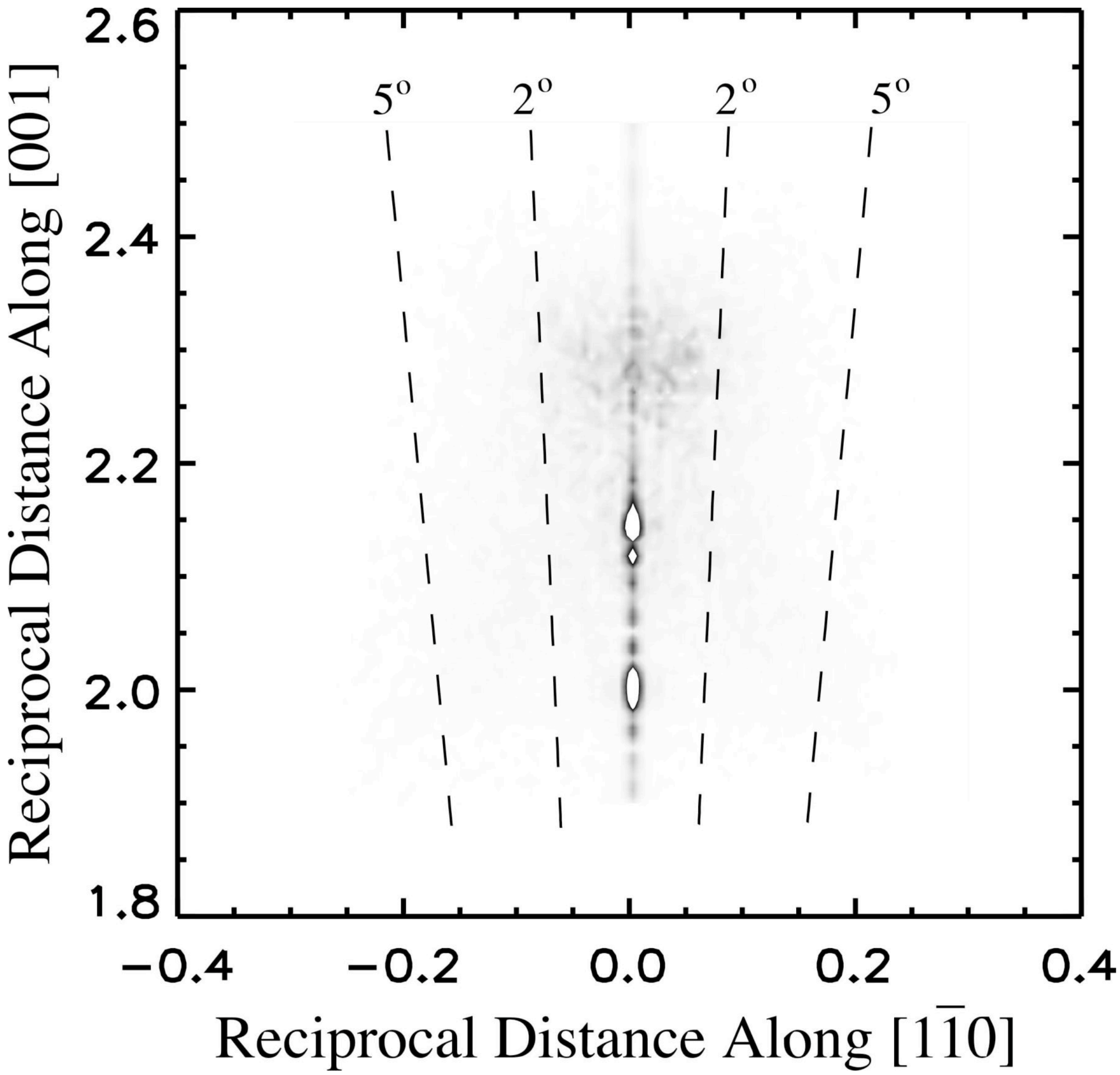

Figure 3.2.4: An expanded view of the $(002)_{BCC}$ / $(2\bar{1}\bar{1}0)_{HCP}$ diffraction peak in reciprocal space. The broadening of the spot associated with the HCP phase is not consistent with a rotation between the HCP and BCC lattice orientation required by the slip/shear mechanism.

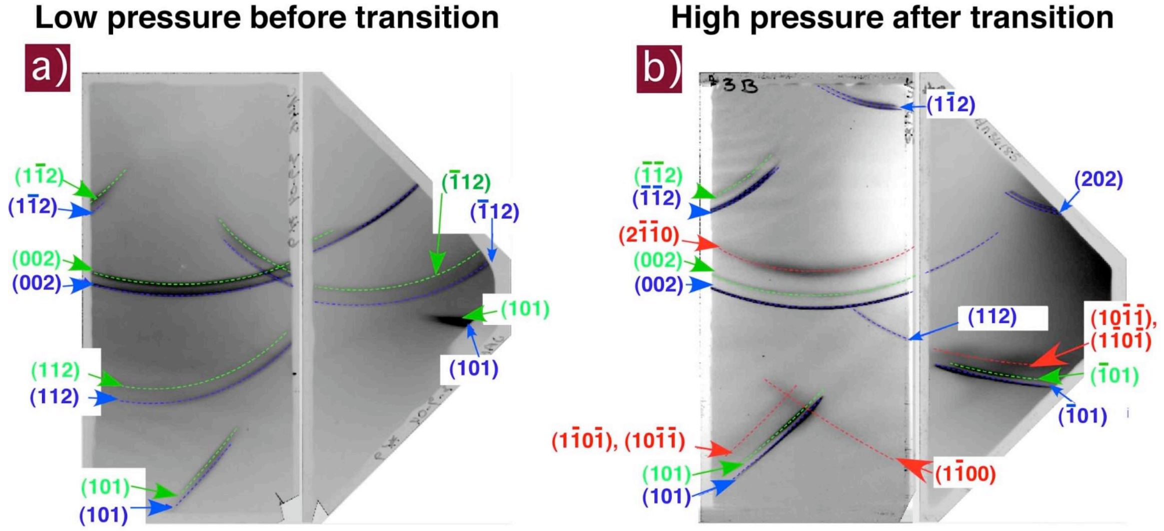

Figure 3.2.5: In situ diffraction data from melt-grown, single-crystal iron shocked along the [100] direction. In a single pulse measurement, we obtain signal from many compressed and static planes, which are labeled with their corresponding Miller indices. Some features are identified with more than one label due to degeneracy of planes. The static BCC and HCP lattice lines are denoted by the blue, green, and red lines, respectively. **(a)** 5 GPa below the transition. The lattice in these samples shows no plastic relaxation below the transition. **(b)** 28 GPa above the transition.

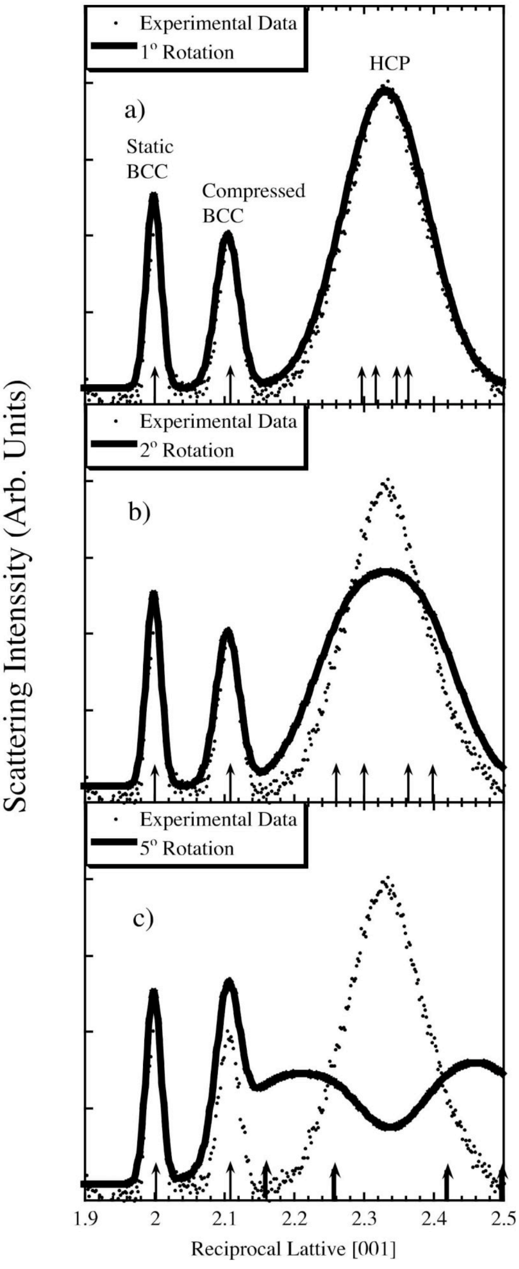

Figure 3.2.6: Lineouts from experimental data showing the compression of the $(002)_{BCC}$ lattice plane fitted by various degrees of rotation between the HCP and BCC lattices. We observe that the width of the fitted line exceeds that of the experimental lineout beyond 2° . The vertical arrows denote the center position of each diffraction line.

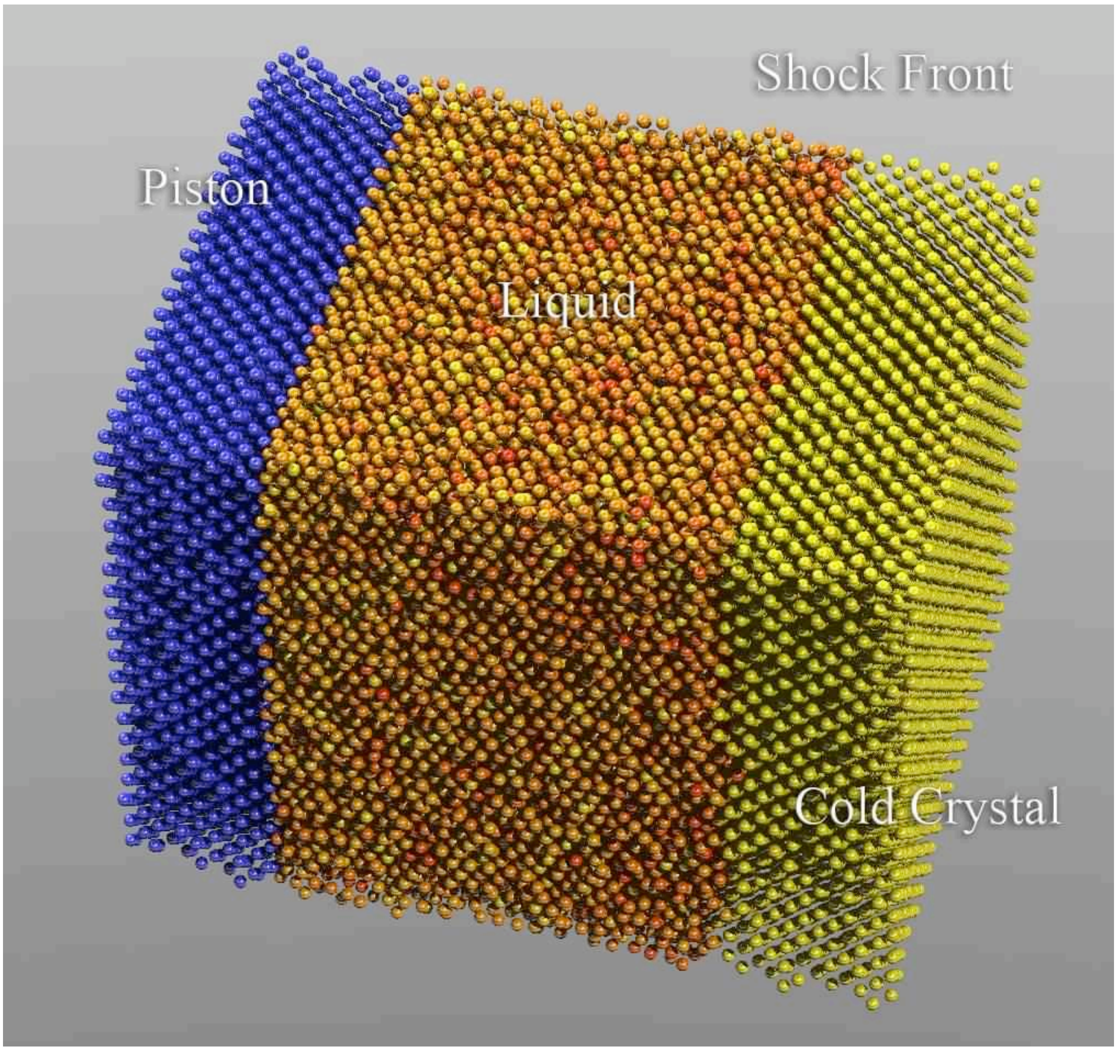

Figure 4.1.1: Snapshot of MD simulation of Cu shocked to 300 GPa along the [100] direction. The blue region corresponds to the piston region constrained to move at a fixed speed of 3 km/sec. The yellow is the pristine unshocked copper atoms, and the orange (color scaled by the centro-symmetry parameter) shows the region where the periodic lattice has melted into a liquid.

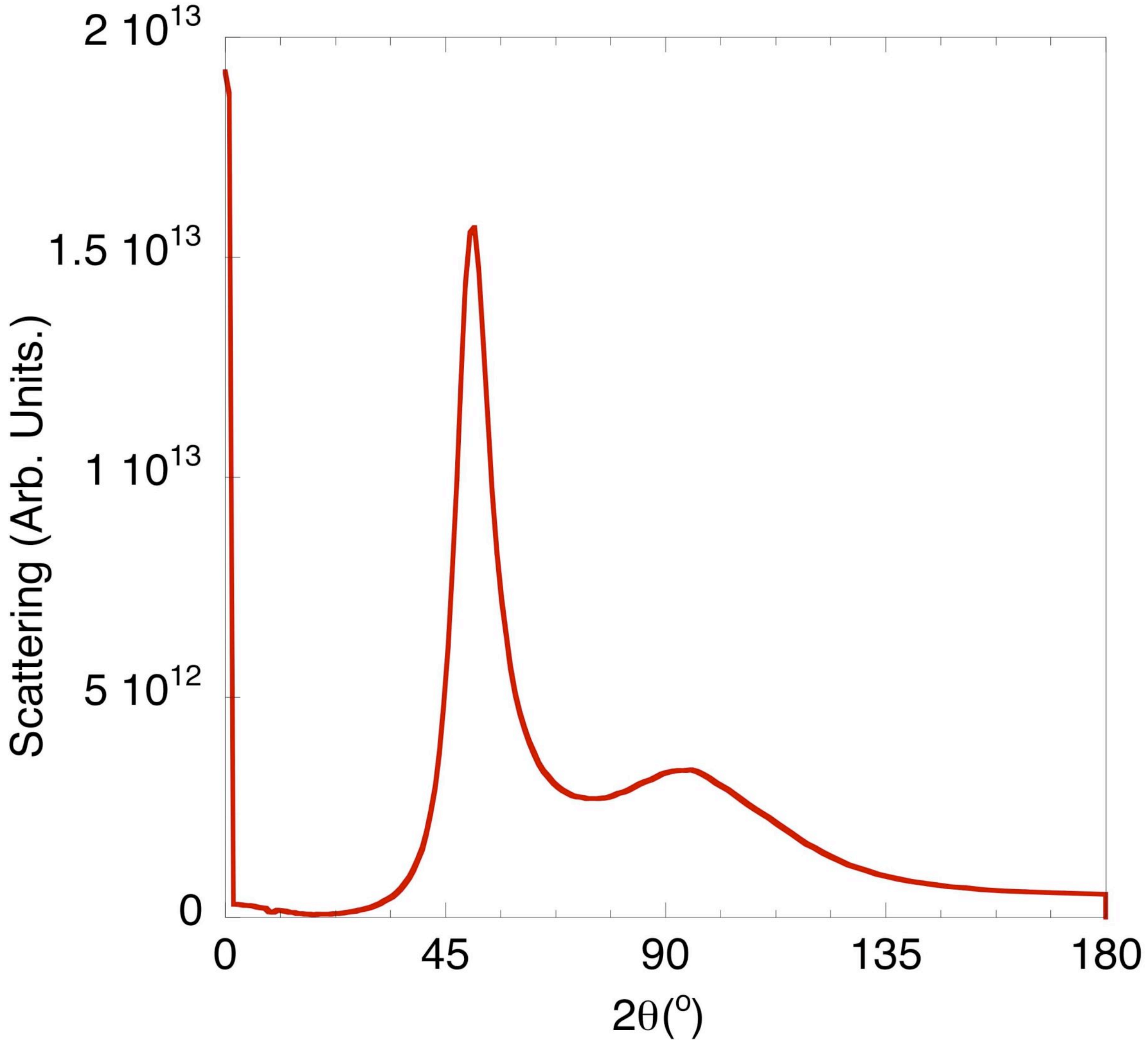

Figure 4.1.2: Simulated x-ray scattering from the molten region of the MD simulation, showing broad features associated with amorphous systems. These features give insight into the correlations in the high pressure fluid.

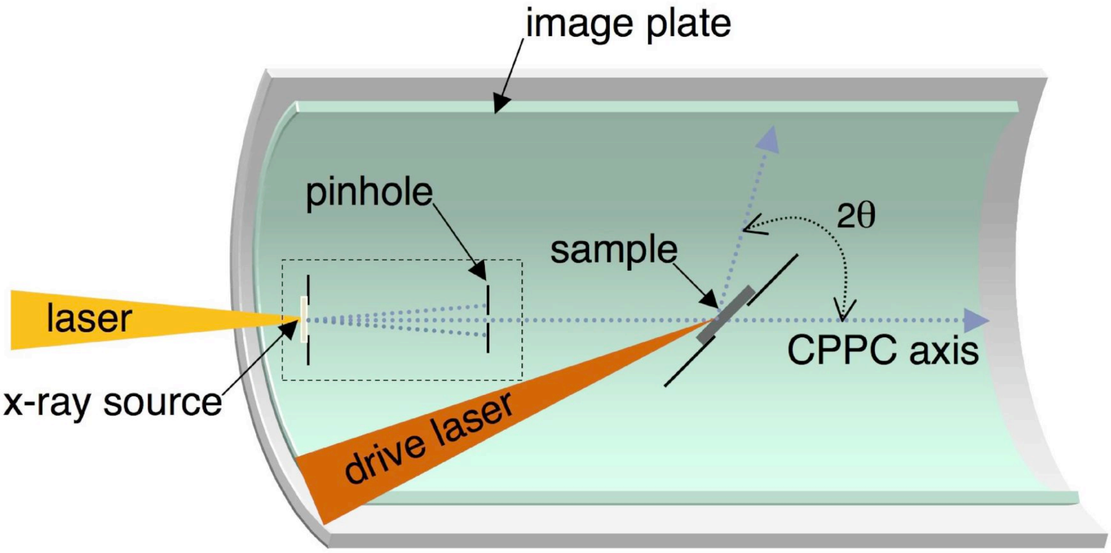
image plate
pinhole
sample
2θ
laser
x-ray source
CPPC axis
drive laser

Figure 4.1.3: Cross sectional view of the cylindrical pinhole powder camera designed for dynamic x-ray diffraction studies of polycrystalline and amorphous materials [Hawreliak 2007]. The cylindrical design can record diffraction rings from angles as low as $2\theta = 30^{o}$ to as high as 150°. The design uses a laser produced plasma as an x-ray source and an ablative laser drive to shock compress the sample.

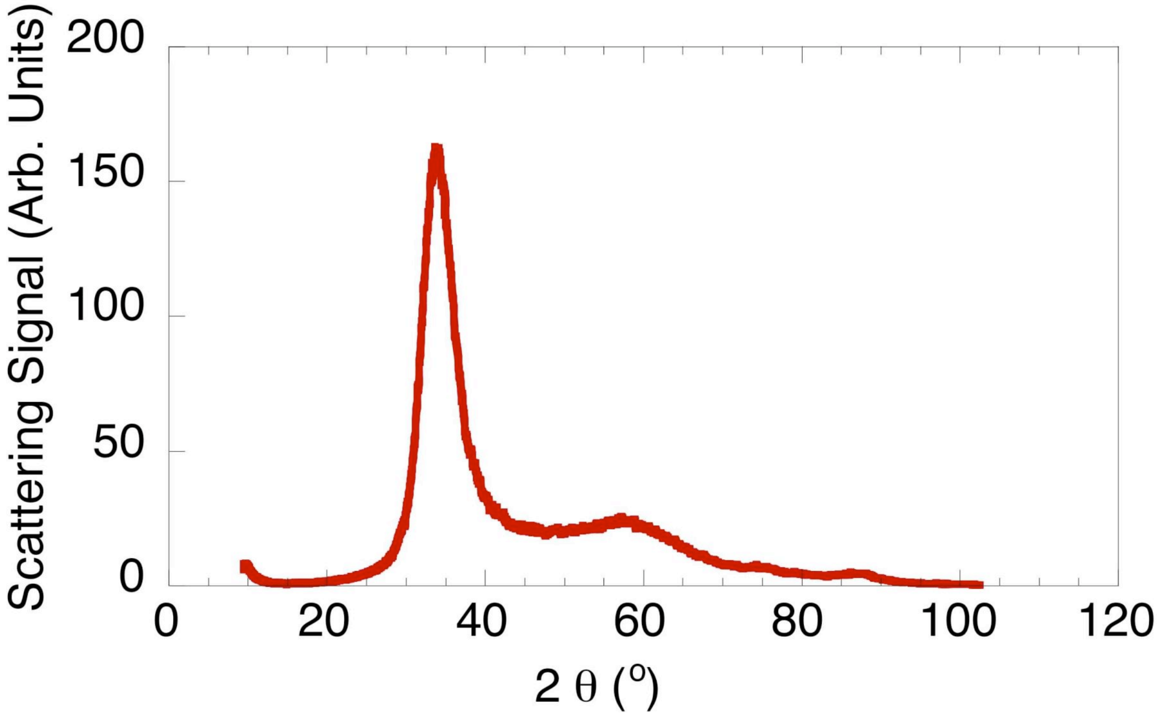

Figure 4.1.4: Nanosecond single-shot amorphous diffraction from uncompressed metallic glass. The signal-to-noise of the instrument suggests it should be possible to experimentally measure the amorphous features of a fluid system under dynamic compression.

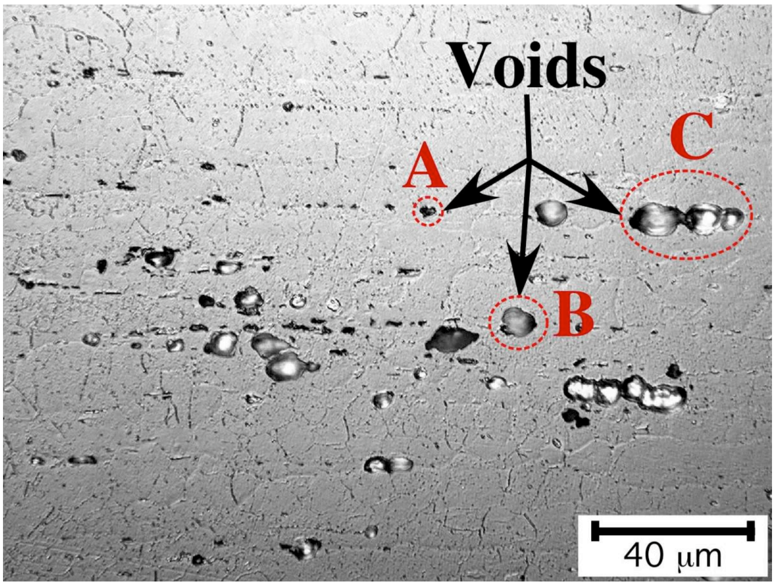

Figure 4.2.1: Micrograph of voids in shock-recovered, incipiently spalled aluminum. During passage of the release wave, these voids grow and may coalesce, resulting in failure.

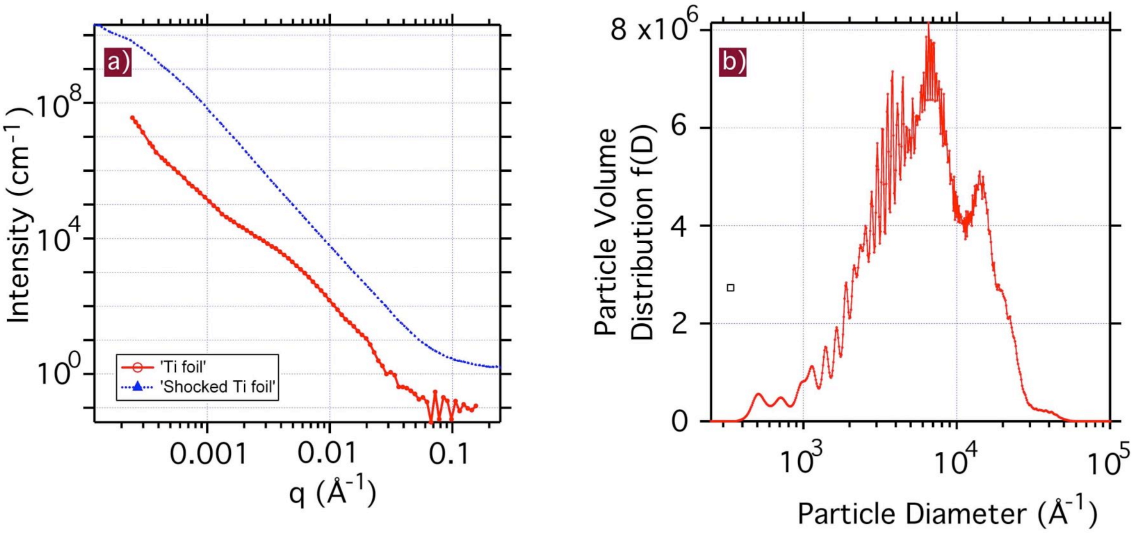

Figure 4.2.2: Static SAXS measurements of recovered titanium and analysis of data. **a)** SAXS data of recovered laser shocked and unshocked Ti samples. **b)** Void distribution assuming spherical voids calculated using maximum entropy algorithm.

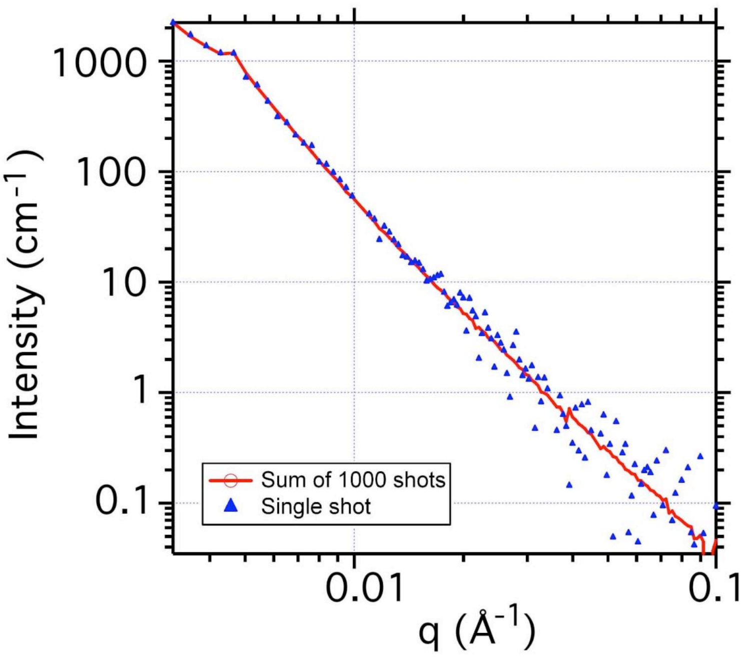

Figure 4.2.3: Comparison of SAXS spectra collected on an unshocked Ti foil in a single 100 ps shot with a sum of 1000 shots.

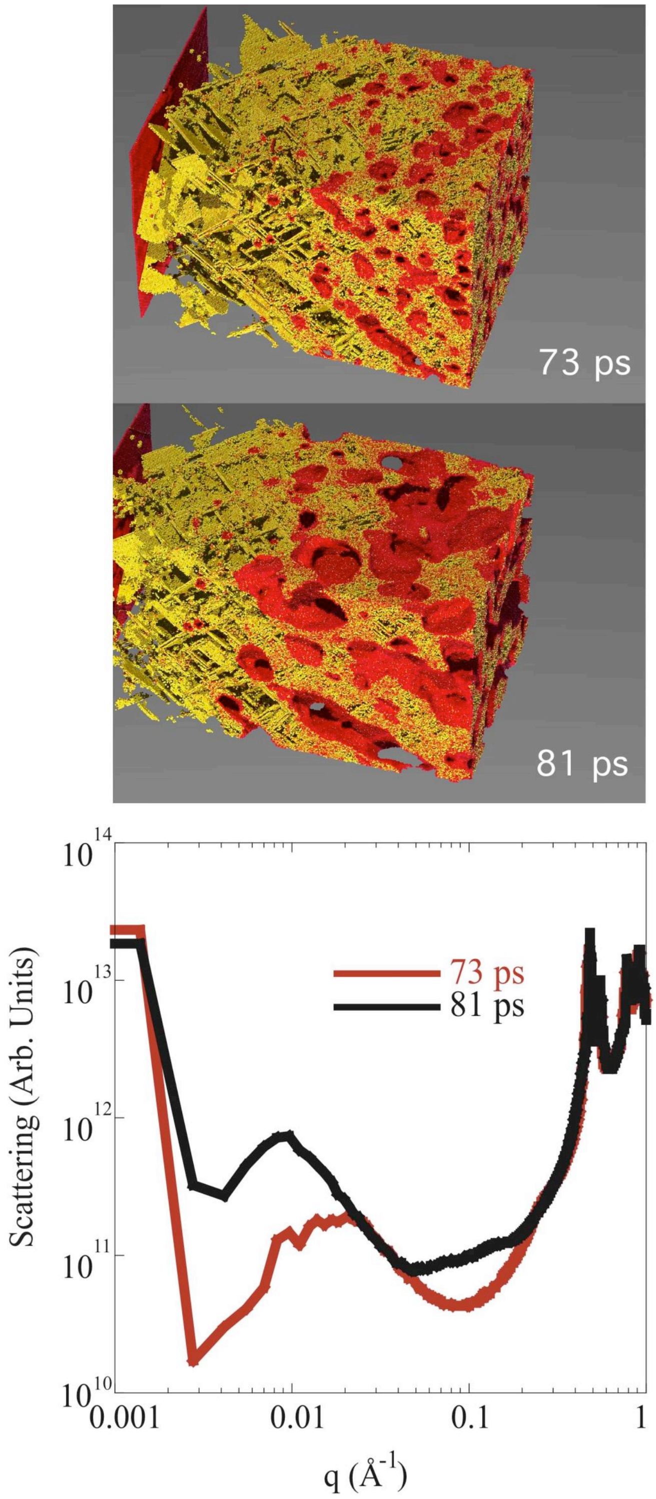

Figure 4.2.4: A plot of the simulated SAXS from MD simulations with voids being generated in single crystal copper released after being dynamically loaded to ~90 GPa. The scattering is shown 13 ps and 21 ps after the pressure has been relieved. At top are real space images of the MD simulation showing the void morphology. The atom color is scaled by central symmetry parameter to accentuate the defects and voids.